

# Single-Step Chemical Vapor Deposition Growth of Platinum Nanocrystal: Monolayer MoS<sub>2</sub> Dendrite Hybrid Materials for Efficient Electrocatalysis

*Wenshuo Xu<sup>1,2</sup>, Sha Li<sup>1</sup>, Gyeong Hee Ryu<sup>1</sup>, Peng Tang<sup>1</sup>, Mauro Pasta<sup>1,2</sup>, Jamie H. Warner<sup>3,4,5\*</sup>*

<sup>1</sup>Department of Materials, University of Oxford, Parks Road, Oxford, OX1 3PH, United Kingdom

<sup>2</sup>Oxford Suzhou Centre for Advanced Research, 388 Ruoshui Road, Suzhou 215123, Jiangsu Province, P. R. China

<sup>3</sup>Walker Department of Mechanical Engineering, The University of Texas at Austin, 204 East Dean Keeton Street, Austin, Texas, 78712, United States

<sup>4</sup>Materials Graduate Program, Texas Materials Institute, The University of Texas at Austin, 204 East Dean Keeton Street, Austin, Texas, 78712, United States

<sup>5</sup>Department of Electrical and Computer Engineering, The University of Texas at Austin, 2501 Speedway, Austin Texas, 78712, United States

\*jamie.warner@austin.utexas.edu;

## ABSTRACT

Two-dimensional (2D) molybdenum disulfide (MoS<sub>2</sub>) has excellent electrocatalytic behavior for the hydrogen evolution reaction (HER), where the catalysis of 2H phase originates from its edges, defects, and strains. Most synthetic methods to activate the electrochemically inert basal planes with catalytic active metals are completed by sequential steps. However, this is extremely time-

consuming and lacks production scalability. Herein, we develop a one-step strategy to achieve efficient electrocatalyst of Pt:MoS<sub>2</sub> hybrid utilizing atmospheric pressure chemical vapor deposition synthesis on a conductive glassy carbon (GC) plate that can be directly employed as the working electrode in the HER. The monolayer thickness ensures decreased interlayer electron hopping and increased efficiency of the charge transfer from the electrode. We tune the domain morphology by controlling the precursor flux to enter kinetic or thermodynamic growth regime, delivering dendritic or triangular shape. The materials chemistry undertaken provides fundamental insights into the instability of Pt as metal substitutional dopants in the MoS<sub>2</sub> lattice, and instead the stable configuration observed is with Pt as highly dispersed small nanocrystals and single atoms bound to the MoS<sub>2</sub> surface. The Pt functionalization at a reduced loading level modulates the favorable HER pathway and triggers synergies in the cocatalyst, which exhibits onset potential of 48 mV, Tafel slope of 46 mV dec<sup>-1</sup>, and exchange current density of 110  $\mu\text{A cm}^{-2}$ . The enriched edges and defects of dendrite endow it superiority to the triangle, with regard to the density of catalytic sites, synergistic effects, along with electrical resistance. These underpin the positive role of large dendritic MoS<sub>2</sub> monolayer as Pt scaffold in water electrolysis.

## INTRODUCTION

Efficient hydrogen evolution via water splitting is an eco-friendly way to generate clean energy.<sup>1,2</sup> This is typically achieved by involving electrocatalysts to reduce the overpotential of the reaction.<sup>1</sup> Platinum on carbon (Pt/C) displays the highest catalytic activity for the HER with a near-zero overpotential, but its use has been subject to the scarcity of natural resources.<sup>3</sup> Given the good accessibility and outstanding electrocatalytic properties of MoS<sub>2</sub>, it has been considered as a promising candidate to replace the costly Pt metal.<sup>4</sup> The exposed edges of MoS<sub>2</sub> have been proven

to be electrocatalytically active for HER,<sup>5</sup> attracting intense efforts on the design of its morphology.<sup>6–11</sup> Till now, enhanced HER performance has been realized by a variety of MoS<sub>2</sub> nanostructures rich in edges, such as porous frameworks,<sup>6,7</sup> vertically aligned atomic layers,<sup>8</sup> randomly oriented nanoflakes,<sup>9</sup> and so on.

Chemical vapor deposition (CVD) has been extensively adopted to yield large-scale two-dimensional (2D) materials for industrial uptake. Nonetheless, distinct from the edges, the semiconducting basal plane of the 2H-phase MoS<sub>2</sub> prepared by CVD is electrochemically inert, rendering it inferior to the metallic 1T-phase MoS<sub>2</sub> in the HER, for which the synthesis approach (e.g., solution-based lithium intercalation) is unscalable.<sup>12–14</sup> Taking these into consideration, diverse approaches have been attempted to activate the basal plane of atomically thin MoS<sub>2</sub> grown by CVD, which include defect engineering,<sup>15,16</sup> metal doping,<sup>17</sup> strain applying,<sup>15</sup> field tuning,<sup>18</sup> and MoS<sub>2</sub>–substrate interaction optimizing.<sup>19</sup> It has also been corroborated that hybridizing MoS<sub>2</sub> with other materials can accelerate the electron transport and/or introduce synergies, therefore enhancing the HER kinetics.<sup>20–24</sup> These can improve the catalysts' efficiency, but have at least one of the following drawbacks: (1) complicated preparations are often required prior to the applications;<sup>25</sup> (2) some physical properties of MoS<sub>2</sub> are sacrificed due to the damage to its crystal lattice;<sup>15,16</sup> (3) the HER efficiency of such noble metal-free catalysts discovered so far are generally poorer than those comprising Pt.<sup>26,27</sup> In terms of the hybrid nanocomposites, the microstructure and dispersion of the particles along with their interaction with the support deserve extra attention considering the possibility of agglomeration, which would decrease the hybrid's electrocatalytic activities and durability.<sup>27,28</sup> Earlier report has elucidated that introducing single heteroatoms and metal clusters in MoS<sub>2</sub> can modify its electronic structure, whereby bringing excellent catalytic performances.<sup>29</sup> Thus, an inclusion of Pt is still favored to yield highly efficient MoS<sub>2</sub>

electrocatalysts, and the structural optimization of Pt would be crucial to minimize the needed mass. For this, one can downsize the loaded Pt species and facilitate their dispersion across a certain support, so as to increase the electrochemical active surface area and obstruct the nanoparticles from sintering, thereby improving the catalyst's activity and durability. The microstructure of the Pt nanocrystals atop pre-grown MoS<sub>2</sub> monolayer has been shown,<sup>7,30</sup> yet doping 2D crystals down to the nanoscale during their CVD synthesis has remained challenging, especially while building a scaffold rich with catalytic sites at the same time. More importantly, the interactions between transition metal dichalcogenides (TMDs) and noble metal dopants along with the HER mechanism of the as-attained electrocatalysts have not been unveiled thoroughly.

In this work, we explore the direct hybridization of large and stable Pt:MoS<sub>2</sub> dendrite cocatalysts on an HER electrode using a scalable synthetic technique. The growth is controlled to prevent the formation of Pt:Mo alloys, where the Mo atoms are electrochemically inert. Our strategy delivers dendritic shape and monolayer nature of MoS<sub>2</sub>, offering high densities of catalytically active centers (i.e., its edges and defects) and maximized charge transfer. The Pt species are stabilized on the MoS<sub>2</sub> as single atoms and nanosized clusters, displaying large specific surface area at low loading. The decorated Pt activates the basal plane of MoS<sub>2</sub>, contributing to enhanced HER activities in conjunction with the edges and defects of MoS<sub>2</sub> and arising synergetic behaviors. The domain morphology, crystal structure, chemical states, and elemental composition are studied by scanning electron microscopy (SEM), annular dark field scanning transmission electron microscopy (ADF-STEM), X-ray photoelectron spectroscopy (XPS), and energy dispersive X-ray (EDX) analysis, respectively. The electrocatalytic performance is investigated in acidic media by linear sweep voltammetry (LSV) and cycling tests. The electrocatalytic behavior

of this special hybrid system is probed, which demonstrates promise as an advanced catalyst for HER.

## RESULTS AND DISCUSSION

Monolayer MoS<sub>2</sub> has been grown by atmospheric pressure chemical vapor deposition (APCVD), which is a scalable method to produce high-quality 2D materials in a controllable manner, without supplemental requirement of vacuum apparatus. Since the highly conductive glassy carbon (GC) exhibiting negligible catalysis is widely used as the working electrode in the HER, it is worth figuring out the synthesis conditions of efficient nanocatalyst on a GC thin plate. This can help to exempt any follow-up procedures such as mechanical transfer and surface cleaning treatment, which always take time plus efforts and deteriorate the properties of the catalyst. Figure 1a illustrates the sample preparation procedures and Figure 1b depicts the CVD setup utilized to grow Pt:MoS<sub>2</sub> hybrids over a large area. We have selected acetone as the solvent for the hexachloroplatinic acid (H<sub>2</sub>PtCl<sub>6</sub>) Pt source, because of its low cost, wide commercial availability, and low boiling point thus enabling a single-step synthesis. The solution is first drop-casted and applied evenly onto the GC surface, then the H<sub>2</sub>PtCl<sub>6</sub> is reduced into Pt metal by the hydrogen (H<sub>2</sub>) gas transported with argon (Ar) through the CVD system. After that, the Pt:MoS<sub>2</sub> dendrites are produced via four stages, as presented in Figure 1c. (1) Nucleation. The formation of MoS<sub>2</sub> nuclei is preferentially initiated around the Pt, attributed to the lower energy barrier at these heterogeneous sites. The introduced H<sub>2</sub> reduces the H<sub>2</sub>PtCl<sub>6</sub> to Pt and might also play a role in the defect engineering of MoS<sub>2</sub> by generating numerous sulfur (S) vacancies, grain boundaries, as well as micro-cracks/holes in the MoS<sub>2</sub> basal plane. These undercoordinated sites are not only catalytically active for the HER,<sup>14–16,25,31</sup> but also display high binding affinity of the doped

Pt.<sup>7,30,32,33</sup> (2) Main growth. Aiming to yield large dendrites, we adjust the growth from thermodynamic mode to kinetic mode via precise control over the relative concentration of the precursors, which is technically realizable by placing the GC support in vicinity of the tube wall. Specific diffusion-limited aggregation (DLA) is driven by a high excess of S vapor compared with the Mo vapor on the substrate surface. In such process, the mass transport coefficient of the gaseous precursors is considerably larger than the reaction rate constant ( $h_g \gg k_s$ ). Consequently, with the diffusion of the reactants being the rate-determining step, highly dendritic structures are produced with small fractal dimension and large domain size.<sup>10,34</sup> To ensure a consistently laminar rather than turbulent flow and permit the growth of uniform monolayer domains, the Reynold's number has been maintained below 200 ( $Re < 200$ ) in the reaction system by controlling the total velocity of the carrier gas flow. (3) Edge attachment. We include this stage to avoid the stacking, given that decreasing the layer number can increase the hopping of electrons from the electrode onto the hybrid surface, whereby facilitating the electrocatalytic activities.<sup>35</sup> The atoms residing on the first grown layer migrate freely and attach to the nearest domain edges, instead of being bound on the surface and forming adlayers. This helps to realize higher thickness uniformity and larger domain size. (4) Thermal annealing, which has been designed to increase the hybrid's stability by enhancing the physisorption at the Pt–MoS<sub>2</sub> interface, which will be discussed in more detail in the electrochemistry section.

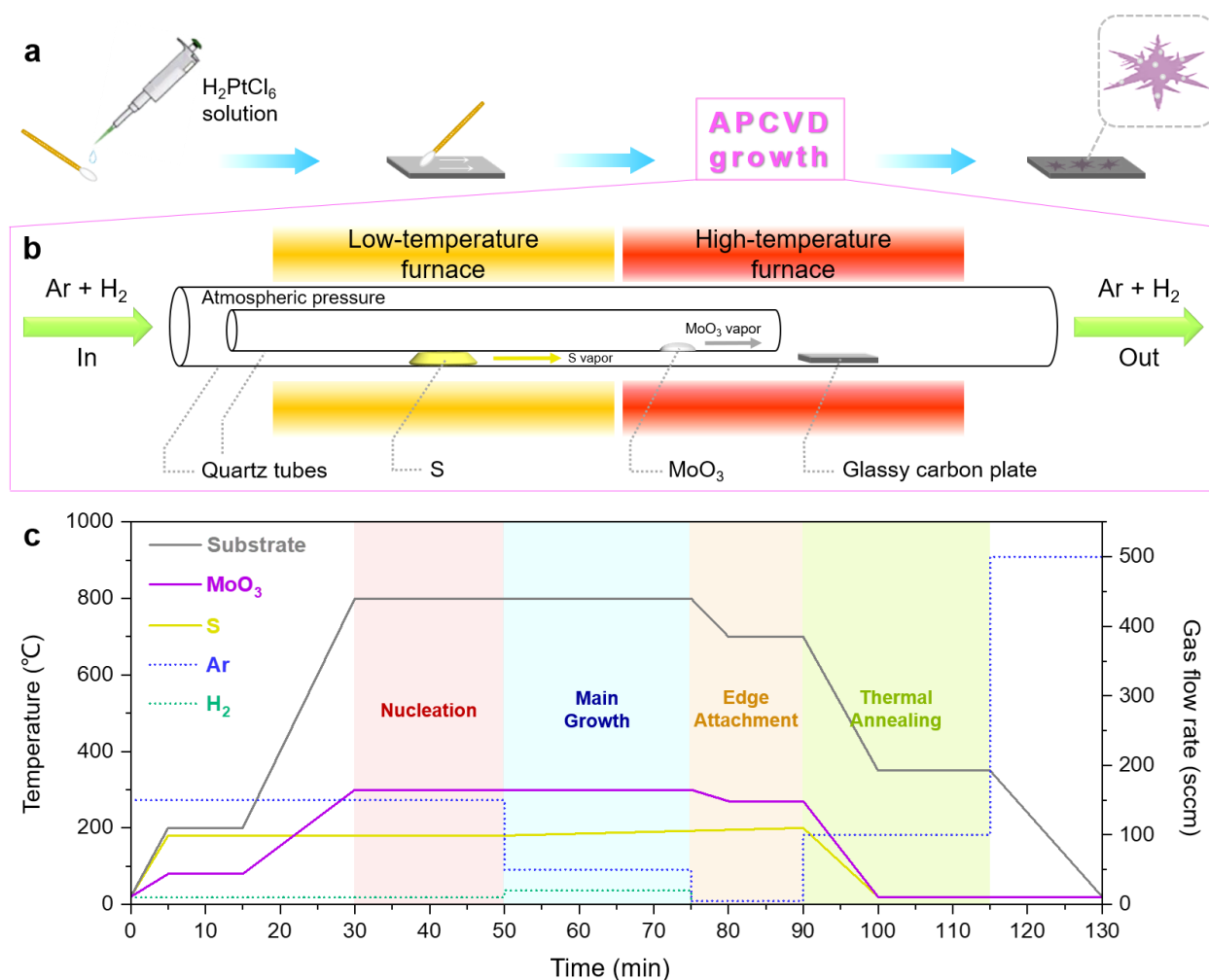


**Figure 1.** Production of the Pt:MoS<sub>2</sub> hybrids. (a) Procedures: drop-casting of  $\text{H}_2\text{PtCl}_6$  acetone solution with a  $\mu\text{L}$  burette onto GC plate surface, application of the solution with cotton tip, APCVD growth, and an as-prepared sample with the silver balls representing the decorated Pt. (b) Schematic diagram of the APCVD reaction system. (c) Programmed temperature and carrier gas flow rate as a function of the time for APCVD.

Figure 2a shows the APCVD-grown Pt:MoS<sub>2</sub> monolayer dendrites, whose large sizes allow high capacity of Pt. The six-fold symmetric backbones of the dendritic MoS<sub>2</sub> domains are also observed for those produced on SiO<sub>2</sub>/Si support.<sup>10</sup> Originating from the cyclic defects in MoS<sub>2</sub> nuclei,<sup>36</sup> these six directions are associated with the hexagonal symmetry of the MoS<sub>2</sub> crystal structure and the three axis of zigzag lattice directions that have different growth rates compared to the arm-

chair directions, and are therefore independent of the growth substrate. The domain thickness has been measured by atomic force microscope (AFM) measurements (Figure 2c–e), and the values of  $\sim 8\text{--}10\text{ \AA}$  are in good agreement with previous studies for monolayer  $\text{MoS}_2$ .<sup>37,38</sup> Figure 2c shows that Pt tends to decorate the edges and grain boundaries of the dendritic  $\text{MoS}_2$  when the doping level is low, whereas these do not happen for pristine  $\text{MoS}_2$  dendrite (Figure S1), proving that the observed features are from the Pt but not  $\text{MoS}_x$  clusters aggregated during the CVD growth. The edges and grain boundaries contain larger numbers of dangling bonds that have a higher affinity for absorbing Pt atoms, which could easily grow/aggregate into Pt nanocrystals/nanoclusters owing to their high mobility across monolayer  $\text{MoS}_2$ .<sup>7,33</sup> The SEM image of the triangular-shaped Pt: $\text{MoS}_2$  hybrids are displayed in Figure S2, where the Pt nanoclusters are deposited on both the GC substrate and the  $\text{MoS}_2$  surfaces. At heavy Pt loading  $>5\text{ wt \%}$ , however, a stable intermetallic Pt:Mo compound is formed along the Pt–Mo phase diagram.<sup>39</sup> As a result, no defined 2D structure but small isolated bulky crystals are grown (Figure S3).



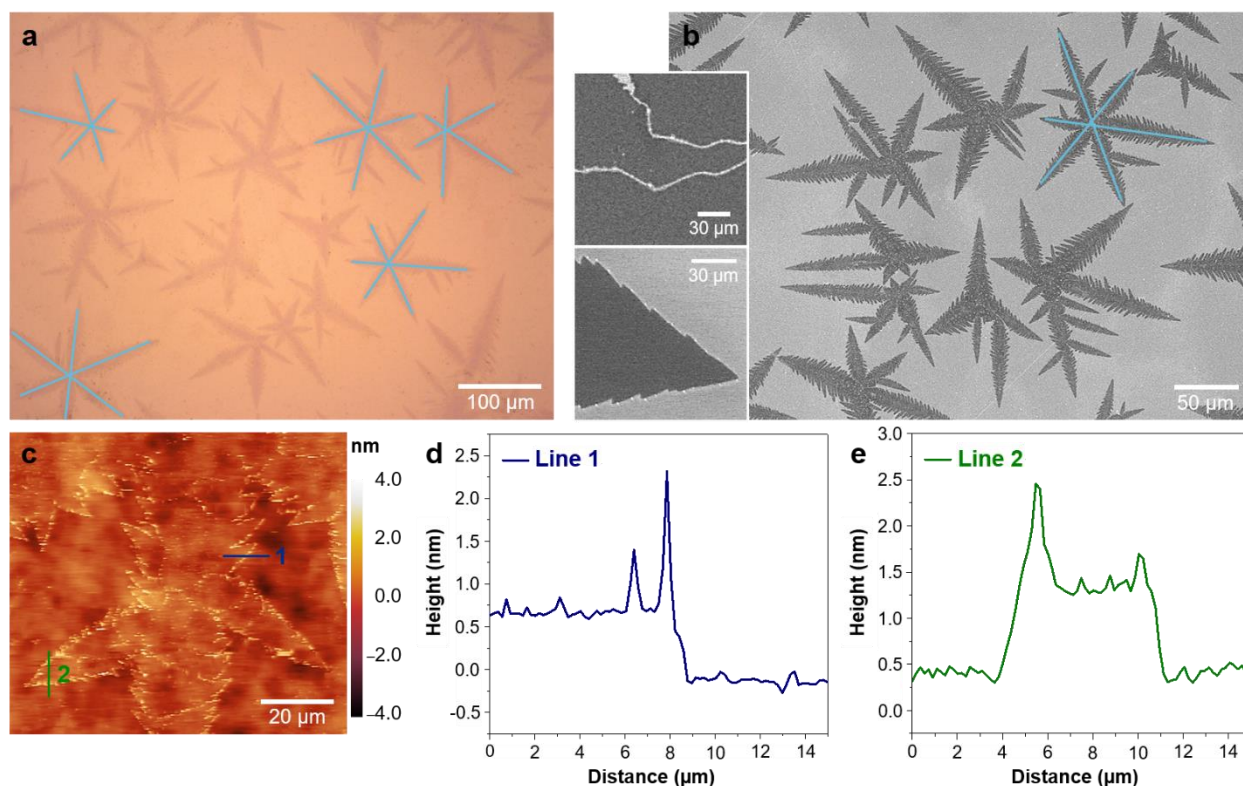


**Figure 2.** (a) Optical microscopic image and (b) SEM image of the APCVD-grown monolayer MoS<sub>2</sub> dendrites. Insets: magnified SEM images showing the Pt nanoparticles at the grain boundaries (upper panel) and the edges (lower panel). (c) AFM image and the (d,e) height profiles corresponding to the lined regions in (c).

Next, we have conducted XPS to understand the chemical transformations during the APCVD process via the information on product's elements and their valence states (Figure 3). Thanks to the large X-ray beam size with a diameter of 400  $\mu\text{m}$ , which can cover the whole dendrite, we are able to quantify the elemental ratio of Pt to Mo in the as-received hybrids by averaging 5 tested domains. Normalized atomic percentages can be acquired from the areas of the elemental peaks detected through a survey scan (Figure 3a), following background subtraction and application of sensitivity factors. The Pt content has been confirmed to be 5 wt % in this case.

Apart from the characteristic peaks of Mo and S, the observation of Pt peaks validates its presence in the MoS<sub>2</sub>. The peak position values are displayed in Table S1, echoing the reported data.<sup>32,40,41</sup> The Mo<sup>6+</sup> ionization state is ascribed to the MoO<sub>3</sub> precursor that has not been sulfurized during the APCVD or local oxidized regions of the sample after exposure to air. The Mo 3d peaks of Pt:MoS<sub>2</sub> dendrite are downshifted by 0.3 eV relative to those of pristine MoS<sub>2</sub> (Figure 3b), indicating that the Mo atoms gain electrons as a consequence of the Pt incorporation. Moreover, downshifts of 0.2–0.3 eV and upshifts of 0.2 eV in the binding energy are respectively observed for the S 2p peaks (vs pristine MoS<sub>2</sub>, Figure 3c) and Pt 4f peaks (vs pure Pt metal, Figure S4e), which should result from the bonding effects between Pt and S. The modified electronic state density of S can improve the HER behavior of the neighboring Mo.<sup>42</sup> The n-type doping in Mo is verified by the shifts of Mo 3d peaks (Figure 3b),<sup>43</sup> which raises its hydrogen capturing ability. In contrast, first-principles density functional theory (DFT) calculations have indicated that Pt atoms would prefer binding to the Mo. This discrepancy may be attributed to the distinct hybridization routes. The computational study assumed that the Pt was deposited atop pre-synthesized MoS<sub>2</sub>,<sup>30,44,45</sup> whereas the experimental characterization was performed on the Pt doped simultaneously with the synthesis of MoS<sub>2</sub>.<sup>43</sup> As regards Pt nanoclusters, more favorably binding to the S network is unanimously agreed (Figure 3c),<sup>42,46</sup> which may occur soon after they are formed because of their larger size and lower migration ability.<sup>7</sup> Deriving from these electronic modifications, the valence band edge of MoS<sub>2</sub> is lowered by 80 meV from 0.74 to 0.66 eV (Figure 3e). Similar effect has been observed in the manganese-doped MoS<sub>2</sub>, in which Mn–S bond is formed. The substitutional magnetic element, Mn, accounts for a larger shift of 150 meV.<sup>37</sup> The binding energy differences between the S 2p doublet peaks and between the Pt 4f doublet peaks are changed by 0.1 eV after the Pt decoration, which indicate that the formation of Pt–S bonds

slightly affects the chemical states of these two elements (originally  $S^{2-}$  and  $Pt^0$ ).<sup>47</sup> This also gives rise to the  $Pt^{\delta+}$  peaks deconvoluted via Lorentzian/Gaussian fitting,<sup>22</sup> where  $\delta \approx 2$ ,<sup>48</sup> though the stronger  $Pt^0$  peak implies the dominance of Pt metal. The  $Pt^{\delta+}$  state is believed unrelated to the Pt salt residue,<sup>22</sup> considering that the decomposition temperature of  $H_2PtCl_6$  is far below those in our APCVD process. The binding in Pt:Mo alloy crystals is also analyzed by XPS (Figure S4 and Table S1), where the intermetallic bond induces positive core level shifts for both Pt and Mo.<sup>49</sup>

Our XPS results in Figure 3 and S4 suggest the preferred reaction pathways during the APCVD under different conditions, in accordance with the chemical thermodynamics and kinetics. The binding of Pt has been found to be dependent on its loading density. When there is abundant Pt on the substrate, the vaporous Mo would prefer to bind to the Pt, forming a bimetallic alloy. This is favored over the synthesis of  $MoS_2$ , because the local supply of Pt on the GC substrate exceeds the feedstock of S transported by the carrier gas, and the mean free path of Mo to meet Pt is much shorter than that to meet S. The alloyed Pt:Mo crystal is highly resistant to sulfur,<sup>50</sup> and the impeded sulfurization causes negligible yield of Pt:Mo:S or  $MoS_2$ . When the existing Pt is deficient, the Mo would first react with S owing to the lower activation energy, producing  $MoS_2$ . Then, the S in the resultant  $MoS_2$  can form bonds with the Pt. In the latter case, the APCVD growth of  $MoS_2$  and its hybridization with Pt are two successive but independent processes. We determine by experiments that the threshold of Pt content impacting the thermodynamically favorable reactions is ~5 wt %.

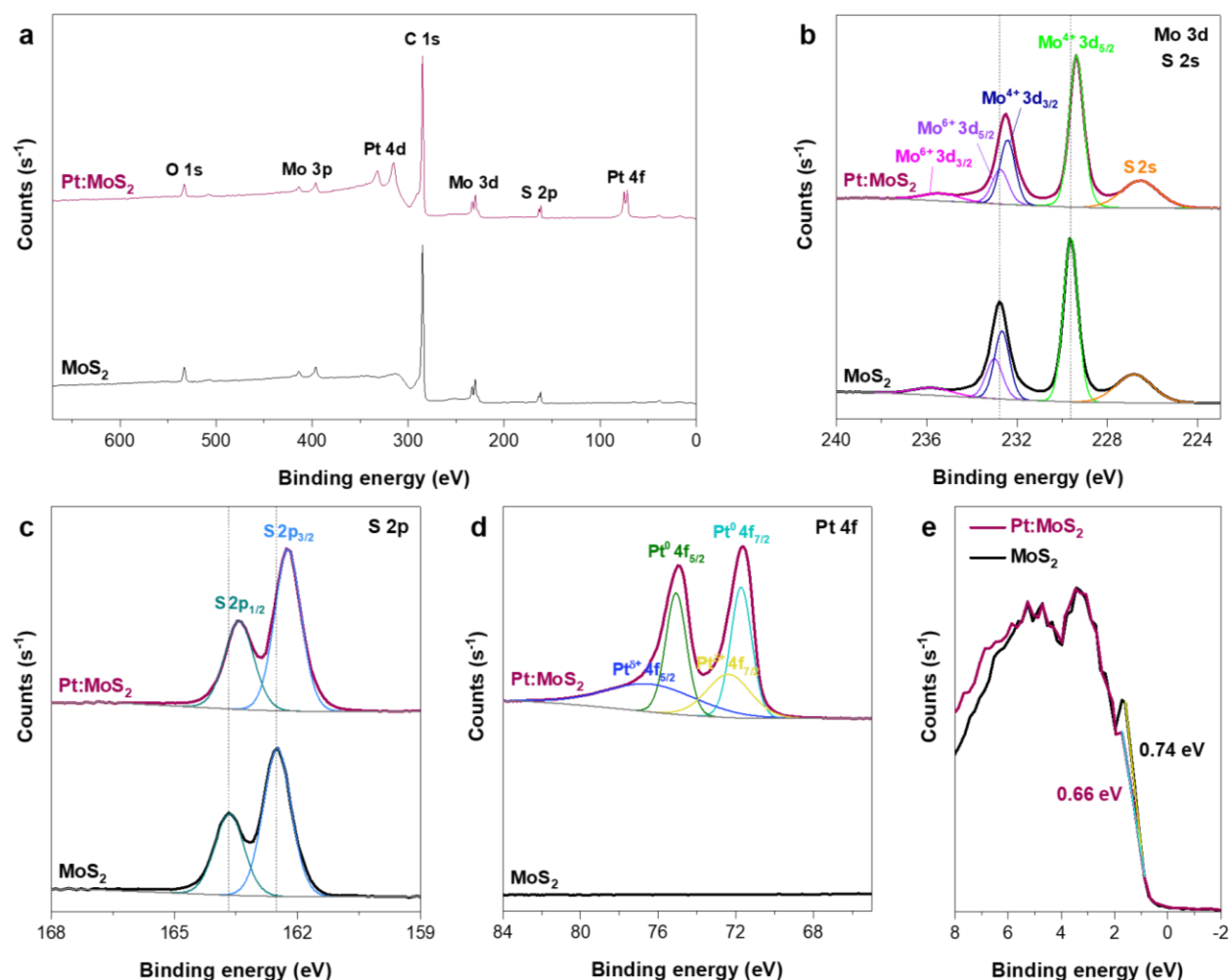


**Figure 3.** XPS spectra of 5 wt % Pt:MoS<sub>2</sub> vs pristine MoS<sub>2</sub> monolayer dendrites on GC thin plates. (a) Survey scans across a wide range to show all the compositional elements. (b–d) Detailed scans for the elemental orbitals of (b) Mo 3d and S 2s, (c) S 2p, and (d) Pt 4f. The peaks are fitted after removing the background, with a combination of Lorentzian and Gaussian functions (L/G = 30%) applied to obtain best fitting outcomes. (e) Valence-band spectra. Linear fits have been applied to show the valence band maximum (VBM) of MoS<sub>2</sub> before and after Pt doping.

The Pt-decorated MoS<sub>2</sub> has been imaged utilizing ADF-STEM to further investigate its atomic and nanoscale structure (Figure 4). At the loading amount of 1 wt %, while a large number of the loaded Pt nanoclusters are dominant and highly dispersed across the MoS<sub>2</sub> basal surface (Figure

4a,b and Figure S6), single Pt atoms have also been achieved (Figure 4f and Figure S5b–d). An interlayer spacing of 0.24 nm has been measured from the corresponding fast Fourier transform (FFT) pattern, Figure 4c, which is the lattice spacing of a Pt nanocrystal in the (111) direction and consistent with the reported value.<sup>51</sup> It demonstrates that Pt has been crystalized simultaneously with the growth of MoS<sub>2</sub> dendrites. Besides, the reflections associated with the MoS<sub>2</sub> and the Pt[111] align to each other, indicative of an epitaxy between these crystal systems. Consecutive scans reveal that the Pt atoms in Figure 4h have migrated away from the region where they initially sat in Figure 4g. Therefore, they are surface-bound and not substituted in the lattice, that is, Pt does not replace Mo. The energy barrier for a Pt atom to migrate across the surface of a defect-free MoS<sub>2</sub> monolayer is very low (~0.6–0.82 eV) at room temperature, so that random diffusion can be induced by the electron beam irradiation with a high accelerating voltage of 80 kV, till they are immobilized via bond formation.<sup>30,43–45</sup> According to the theoretical prediction, the diffusion rate along  $[10\bar{1}]$  is ~100 times larger than that along  $[1\bar{1}0]$ . Such anisotropy would cause severe agglomeration of the Pt.<sup>44</sup> Notwithstanding, monoatomic and homogeneous Pt distribution has been achieved by experiments (Figure 4f and S5b–d), in which the Pt doping proceeds together with the MoS<sub>2</sub> synthesis.<sup>43</sup> This highlights again the merit of our single-step growth strategy.

We have evaluated the diameter and specific surface area of the MoS<sub>2</sub>-supported Pt nanoparticles based on the ADF-STEM images of several different areas (Figure S6). The high magnification gives enough contrast from the single Pt atoms. By means of Gaussian fitting to the as-plotted distribution histogram in Figure 4i, the average size of the Pt particles is ~5.7 nm. A Gaussian function has been chosen here because it indicates normal distribution. As alternatives, the number averaged ( $\bar{d}_n$ ) and volume/area averaged ( $\bar{d}_{v/s}$ ) diameters have been calculated:

$$\bar{d}_n = \frac{\sum d_i}{\sum n_i} = (5.2 \pm 0.9) \text{ nm} \quad (1)$$

$$\bar{d}_{v/s} = \frac{\sum n_i d_i^3}{\sum n_i d_i^2} = 5.8 \text{ nm} \quad (2)$$

The specific surface area (A) can be well estimated with a simplified equation:

$$A = \frac{6}{\rho \bar{d}} \times 10^3 = 48.2 \text{ m}^2 \text{ g}^{-1} \quad (3)$$

where  $\rho$  is the density of Pt metal, i.e.,  $21.45 \text{ g cm}^{-3}$ ,  $\bar{d}$  is the averaged particle diameter in nm, and A usually takes the unit of  $\text{m}^2 \text{ g}^{-1}$ . Note that  $\bar{d}_{v/s}$  has been regarded preferable to  $\bar{d}_n$  as a measure of A.<sup>52</sup> The chemical composition of our sample is reconfirmed by EDX (Figure 4j). The peaks in the spectrum identify the existence of Pt dopants, Mo and S from  $\text{MoS}_2$ , as well as Si from  $\text{Si}_3\text{N}_4$  holder.



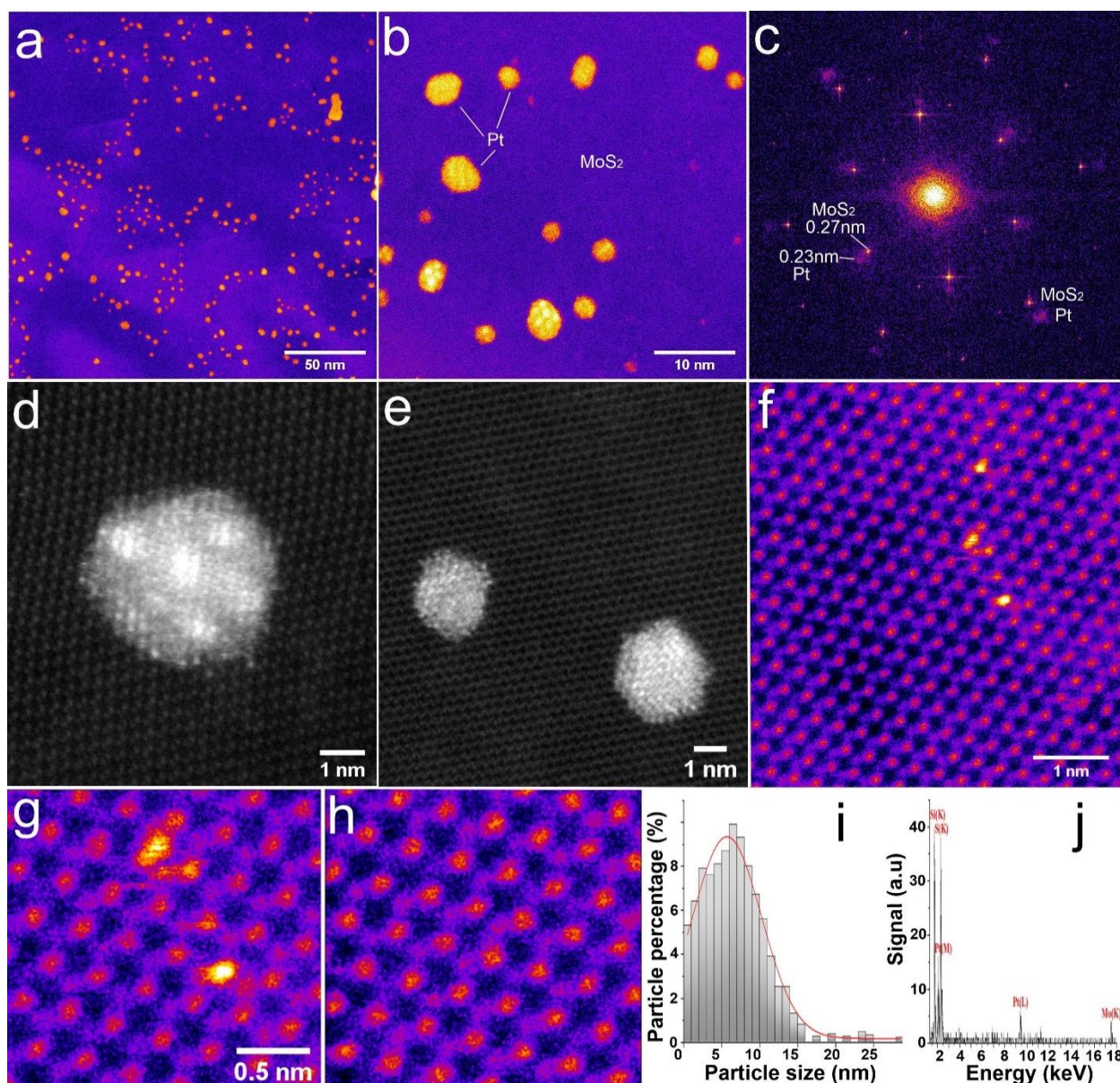


**Figure 4.** Structural and elemental characterization of the Pt:MoS<sub>2</sub> hybrid. (a,b) ADF-STEM images of the basal plane area under (a) lower and (b) higher magnifications. Pt nanoparticles are observed on top of the MoS<sub>2</sub> surface. (c) FFT pattern from the entire image in (b). (d,e) ADF-STEM images of (d) one Pt nanocrystal and (e) two smaller Pt nanocrystals on monolayer MoS<sub>2</sub>. (f) High magnification image showing monoatomic Pt on the MoS<sub>2</sub>. (g,h) Images of the same region between consecutive scans. (i) EDX spectrum. The identified elements (Si, S, Pt, and Mo) along with their respective electronic shells (K, M, and L) are labelled above each peak. (j) Gaussian-fitted histogram illustrating the size distribution of the Pt particles.

We have performed Raman and PL spectroscopies to further study the Pt–MoS<sub>2</sub> interactions and their effects. There are two Raman-active modes corresponding to MoS<sub>2</sub> (Figure 5b), namely, E<sub>2g</sub><sup>1</sup> at ~384.0 cm<sup>-1</sup> for the in-plane Mo–S phonon and A<sub>1g</sub> at ~403.6 cm<sup>-1</sup> for the out-of-plane Mo–S phonon. The frequency difference of A<sub>1g</sub> – E<sub>2g</sub><sup>1</sup> centering around 19 cm<sup>-1</sup> lends further support to the monolayer thickness of the dendrite.<sup>53</sup> Additionally, the Pt-caused blue shifts of both A<sub>1g</sub> and E<sub>2g</sub><sup>1</sup> peaks may arise from compressive strain and/or p-doping in the MoS<sub>2</sub>.<sup>54,55</sup> The development of compressive strain is ruled out considering that the lattice constant of Pt is larger than that of in-plane 2H-MoS<sub>2</sub>, and the p-doping will be reaffirmed based on the PL characteristics. The surface roughness of MoS<sub>2</sub> can be suggested by the integrated Raman intensity ratio of A<sub>1g</sub>/E<sub>2g</sub><sup>1</sup>, as the A<sub>1g</sub> and E<sub>2g</sub><sup>1</sup> modes are preferentially excited for edge and terrace terminations, respectively.<sup>8</sup> The higher ratios of the hybrids signify that the Pt decoration results in rougher surfaces.

Strong PL is observed in the monolayer MoS<sub>2</sub> upon laser excitation owing to its direct bandgap,<sup>38</sup> while comparatively, Pt doping leads to quenched peak intensity and red-shifted peak position (Figure 5c). To reveal the Pt influences on the excitonic emissions, we have applied Lorentzian fitting to the PL curves for increasing Pt contents (Figure 5d–f). Since localized states (LS) are induced by the structural disorders in MoS<sub>2</sub> nanosheets, the enhancement of LS peak with increasing Pt content implicates the additional lattice defects introduced by the hybridization, which result in quenching and red shift of the PL peak.<sup>56</sup> Another reason could be that the local electronic states are changed by the metallic Pt, thus affecting the band formation of MoS<sub>2</sub>.<sup>57</sup> The presence of negatively charged A excitons (A<sup>-</sup>, also known as trions) demonstrate the n-doping in the MoS<sub>2</sub>, originating from the GC supporting substrate and/or the chemical binding to the Pt. The



relative population densities of A and A<sup>-</sup> can be gained by comparing the integrated intensity of their peaks.<sup>58</sup> The increasing A/A<sup>-</sup> ratio with the Pt loading is suggestive of the Pt-induced p-doping in the MoS<sub>2</sub> under light excitation. This is because the Fermi level of Pt is lower compared with that of MoS<sub>2</sub>, so that a band offset is formed at the Pt–MoS<sub>2</sub> heterojunction and the electrons are transferred from the MoS<sub>2</sub> semiconductor to the Pt metal upon photoinduction.<sup>22</sup> The changes in the MoS<sub>2</sub> spectroscopic features caused by the Pt decoration therefore offer feasibilities of roughly probing the Pt location via Raman and PL mapping. It is notable that the quenching at the MoS<sub>2</sub> edges seen from the Raman and PL intensity maps has no association with the loaded Pt (Figure 5g,h), since this is a typical phenomenon for TMD isolated domains, relying on the smallest laser spot size that can be reached, i.e., ~1  $\mu\text{m}$  by our equipment.<sup>59</sup> The grain boundaries on the dendrite basal surface cannot be visualized in this way because of our detection limit, otherwise we might observe increased PL intensity and decreased Raman intensity at the same position.<sup>60</sup> Nevertheless, this does not affect the identification of Pt nanoclusters sitting on the grain boundaries. The differentiated A-exciton PL peak intensity and position (Figure 5h,i), as well as the Raman peak intensity, which is less affected due to the relatively weak signals (Figure 5g), manifest that Pt has decorated the basal plane of the MoS<sub>2</sub> dendrite, consistent with the ADF-STEM observations (Figure 4, Figure S5 and Figure S6). In comparison, pristine MoS<sub>2</sub> dendrite shows uniform Raman and PL signals across its surface.<sup>10</sup>

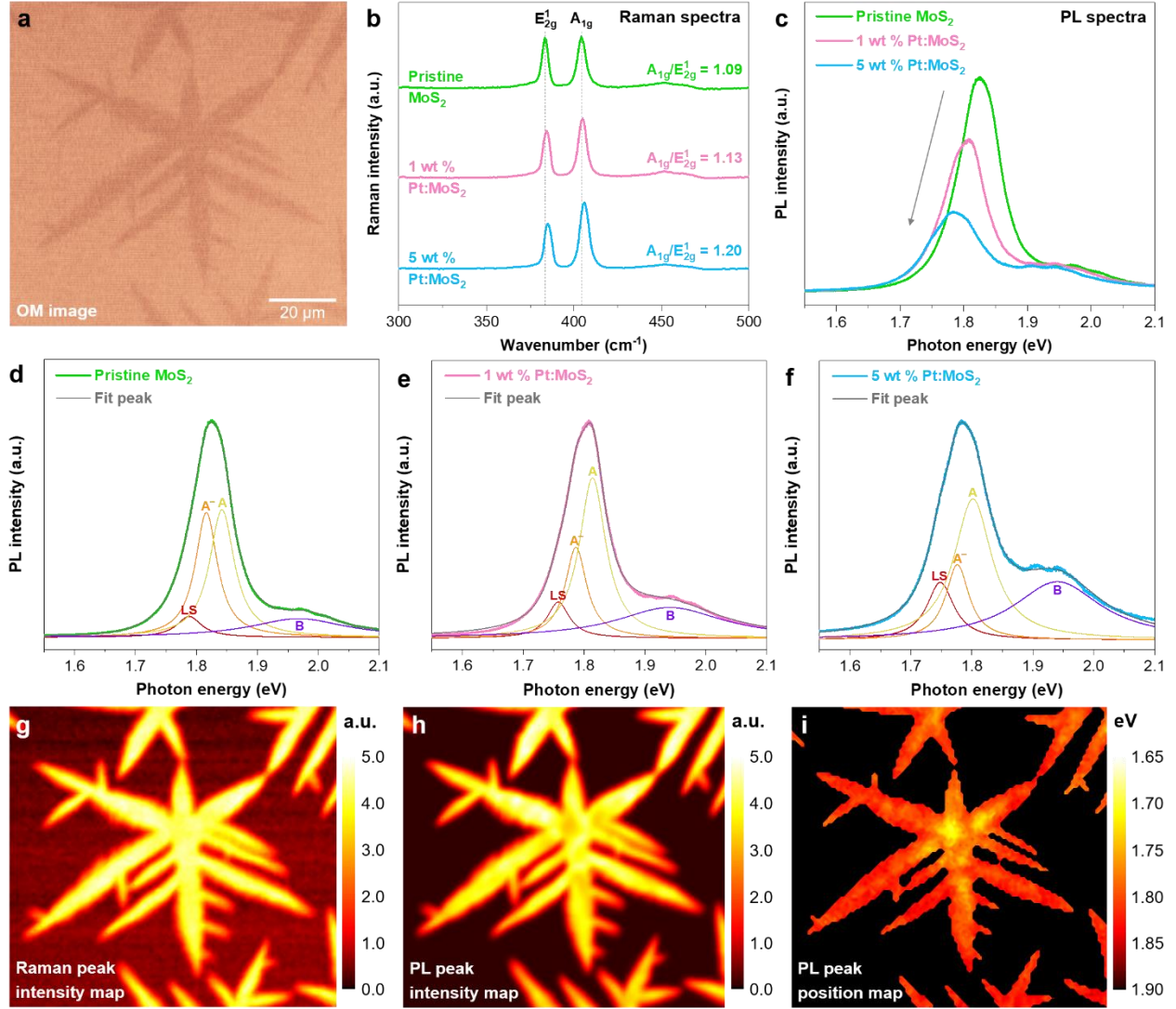


**Figure 5.** Raman and PL spectroscopies of the CVD-grown dendritic monolayer Pt:MoS<sub>2</sub> hybrids and pristine MoS<sub>2</sub>. (a) Optical microscopic image of a typical dendrite for the measurements. (b) Raman and (c) PL spectra. (d–f) Deconvolution for the PL curves in (c), which correspond to (d) pristine MoS<sub>2</sub>, (e) 1 wt % Pt:MoS<sub>2</sub>, and (f) 5 wt % Pt:MoS<sub>2</sub>, revealing the emissions of B excitons (B), A excitons (A), negatively charged A excitons (A<sup>-</sup>), and localized states (LS). Lorentzian functions are utilized for best fitting results, with each coefficient of determination  $R^2 \geq 0.9999$ . (g–i) 2D maps of the dendrite in (a), showing (g) A<sub>1g</sub> Raman peak intensity, (h) A-exciton PL peak intensity, and (i) A-exciton PL peak position.

The electrocatalytic performances of the hybridized Pt:MoS<sub>2</sub> and pristine MoS<sub>2</sub> grown on GC plates with dendritic and triangular shapes have been examined for the HER (Figure 6). All of these MoS<sub>2</sub> are monolayer, ensuring that the interlayer charge barrier is minimal and consistent. Here, we do systematic analysis and provide new insights from several aspects.

**Individual Catalytic Roles of Pt and MoS<sub>2</sub> and Synergistic Effects in the Hybrid.** As shown in Figure 6a,b, the enhanced catalysis by loading Pt (Pt:MoS<sub>2</sub> vs MoS<sub>2</sub>) and by using dendritic scaffold (Pt:MoS<sub>2</sub> dendrites vs Pt:MoS<sub>2</sub> triangles) suggests that Pt works in tandem with MoS<sub>2</sub> for the HER. The superior activities of the hybrids can be explained by two synergies in this system. One occurs between the atomically dispersed Pt species and the Pt(111) nanoclusters. Pt single atoms display maximized specific surface area, whereas Pt nanoclusters show higher conductivity and more efficient HER pathway (Heyrovsky route for Pt atoms vs Tafel route for Pt nanoclusters), hence their copresence on MoS<sub>2</sub> with small separation distance could lead to increased catalytic activities.<sup>61</sup> The other one is between Pt and MoS<sub>2</sub>,<sup>7,42,62,63</sup> manifested by the rapid hydrogen generation stages of 1 wt % and 5 wt % Pt:MoS<sub>2</sub> dendrites (after reaching the overpotentials marked by the navy and olive dashed lines in Figure 6a). For the MoS<sub>2</sub>, the binding of Pt to S would open up its nearest Mo on the basal plane as a new electrocatalytic center.<sup>5,64,65</sup> Furthermore, this bonding behavior could enhance the catalytic properties of both the edge-Mo and the surface-Mo by donating electrons to them (Figure 3b).<sup>42</sup> For the Pt, the MoS<sub>2</sub> offers stabilization sites. When the loading density is low, the Pt would preferentially nucleate and grow or aggregate at the unsaturated sites of MoS<sub>2</sub>, including its edges and grain boundaries (Figure 2b,c).<sup>7,33</sup> At high Pt content, even dispersion is achieved across the MoS<sub>2</sub> basal surfaces and edges (Figure 6g).<sup>7</sup> However, computational analysis has suggested that the metal–support interactions would not affect the HER mechanism or the catalytic activity in a Pt<sub>20</sub>:MoS<sub>2</sub> system.<sup>66</sup> The reason

for this disagreement could be that the Pt<sub>20</sub> is ~6 times on average smaller than the Pt nanoclusters dominantly existing in our hybrids. Hence, the Pt<sub>20</sub>-Pt<sub>20</sub> distance is much shorter for a certain loading amount of Pt, leading to promoted Tafel reaction.<sup>61</sup> Figure S8 summarizes the contributions of Pt and MoS<sub>2</sub> alone and their synergies to the overall HER catalysis.

**HER Kinetics and Mechanism.** (1) Onset potential ( $\eta$ ) is an indicator of the catalyst's activation energy for the HER and can reflect the modulated kinetics. It can be obtained from the Tafel plot in Figure 6b, by identifying the point where the linear relationship  $\eta = b \log |j| + a$  begins. Now we focus on the impacts of Pt loading on the behavior of either triangle or dendrite catalysts. The decreasing  $\eta$  with the Pt content is a sign of the change in electrocatalytically active sites (Figure 6a). The LSV curves indicate that as the overpotential increases, the hydrogen evolution from 1 wt % Pt:MoS<sub>2</sub> can be divided into three stages, whereas two stages are shown by 0.1 wt % and 5 wt % Pt:MoS<sub>2</sub>. For all hybrids, the end of the first stage corresponds to the start of hydrogen production (olive dashed line), and the obviously reduced  $\eta$  signifies the crucial role of Pt in the electrocatalysis. The second stage of 0.1 wt % and 1 wt % Pt:MoS<sub>2</sub> is basically the result of the sole contributions from Pt and MoS<sub>2</sub> entities. The third stage of 1 wt % Pt:MoS<sub>2</sub> (navy dashed line) and the second stage of 5 wt % Pt:MoS<sub>2</sub> exhibit fast release of hydrogen, which can be attributed to the synergistic effects arisen between Pt and MoS<sub>2</sub> in addition to their own performances. These imply that a certain overpotential is required to activate the synergies, and its value reduces with increase in the Pt content. Despite the larger Pt amount, 5 wt % Pt:MoS<sub>2</sub> seems to have comparable synergistic effects with those in 1 wt % Pt:MoS<sub>2</sub>, leading to similar slopes of their LSV curves at high overpotentials. This can be interpreted by the decoration of Pt nanoclusters on the MoS<sub>2</sub> edges and defects. Otherwise such catalytic active regions along with the derived synergistic effects would be retained by their exposure. It is noteworthy that for 0.1 wt % Pt:MoS<sub>2</sub>, some synergistic

behaviors might also take place at increased overpotential, but with a small amount Pt interacting with the MoS<sub>2</sub>, noticeable improvements in the HER efficiency are unlikely to be brought. (2) Tafel slope can suggest the hydrogen evolution rate. It has specific values referring to different elementary reactions: 120 mV dec<sup>-1</sup> for Volmer (adsorption of H<sub>3</sub>O<sup>+</sup> onto a catalytic active site:  $\text{H}_3\text{O}^+ + \text{e}^- \rightarrow \text{H}^* + \text{H}_2\text{O}$ ), 40 mV dec<sup>-1</sup> for Heyrovsky (hydrogen desorption from the catalyst site through an electrochemical reaction:  $\text{H}^* + \text{H}_3\text{O}^+ + \text{e}^- \rightarrow \text{H}_2 + \text{H}_2\text{O}$ ), and 30 mV dec<sup>-1</sup> for Tafel (desorption of H<sub>2</sub> from the catalytic site via combination of two adsorbed hydrogen intermediates:  $\text{H}^* + \text{H}^* \rightarrow \text{H}_2$ ) routes of water-splitting. Volmer–Tafel and Volmer–Heyrovsky are the recognized HER pathways in acidic media. The Tafel slope is evidently decreased after incorporating Pt (Figure 6b), e.g., from 112 to 46 mV dec<sup>-1</sup> by loading 5 wt % Pt onto the MoS<sub>2</sub> dendrites, which indicates a combination of Volmer–Heyrovsky steps for such hybrid cocatalysts. The Tafel plots of 0.1 and 1 wt % Pt:MoS<sub>2</sub> show “curvy” portions with linear Tafel-slope portions in the middle, while these should not be linked to the transition of hydrogen evolution stages. To prove it, we show the results over a wide range (Figure S7), where no more linear correlation is observed. That is, in each plot there is only one approximation to the Butler–Volmer equation and therefore each catalyst has only one Tafel slope. (3) Exchange current density  $j_0$  is commonly used to describe the efficiency of electron transfer in catalysts at zero overpotential. So, it should increase with the improved hybrid–substrate contact resulting from the direct growth and thermal annealing,<sup>19</sup> which will be ascertained later. The value is calculated by fitting the linear portion of the Tafel plot ( $\log j$  vs  $\eta$ ).<sup>5,67</sup>

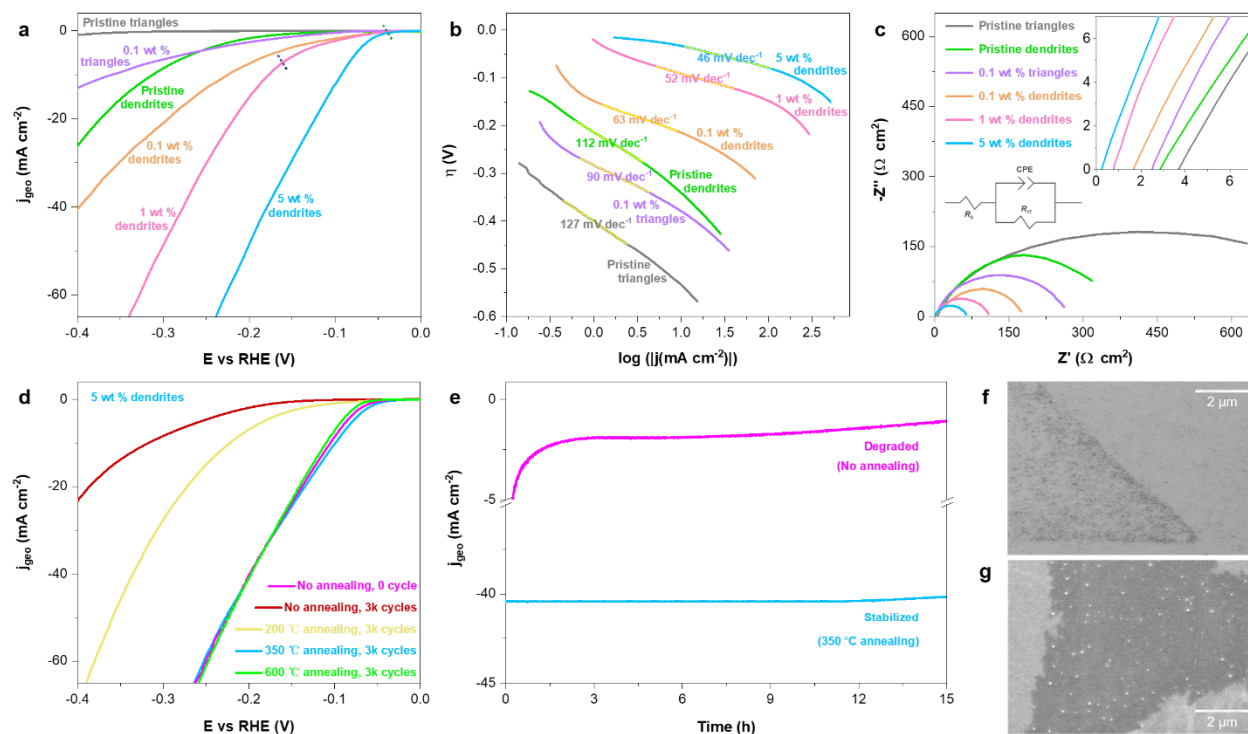


**Figure 6.** HER activities of the dendritic and triangular monolayer MoS<sub>2</sub> with varying Pt contents. (a) Cathodic polarization curves. The current density is normalized to the geometric area of the GC working electrode, denoted by the subscript of “geo”. The transitions in hydrogen evolution stages are marked by the olive and navy dashed lines. (b) Tafel plots with the slopes obtained via linear fits. (c) Nyquist plots at 10 mV DC bias with the frequency swept from 200 000 to 1 Hz, which shows the impedance of the electrochemical system. The left lower inset is a Randles equivalent circuit model, and the right upper inset shows the zoomed-in high frequency region (squared). (d–g) Stability investigation on the 5 wt % dendrite hybrids. (d) Cathodic polarization curves before and after 3,000 cycles for different annealing treatments. (e) Chronoamperometric responses at the overpotential of –0.2 V vs RHE and (f,g) SEM images, which compare the stabilized with the unstabilized samples as a result of long-term cycling.

We correlate these electrocatalytic metrics of the dendrite hybrids to the Pt content quantified by wt % and  $\mu\text{g cm}^{-2}$  (Figure 7a–c). The numbers are listed in Table 1. The dependence of Pt surface area on its loading percentage is substantiated by investigating the current density of

the dendrite hybrids at three overpotentials, i.e.,  $-0.1$ ,  $-0.2$ , and  $-0.3$  V vs RHE (Figure 7d–f). When more Pt is loaded, on one hand, the Pt species would agglomerate into relatively larger particles,<sup>44</sup> so that both its activity per atom and the synergy between Pt nanoclusters and Pt single atoms are diminished. It is worth mentioning that the Pt migration could be facilitated as the overpotential decreases owing to the propulsion by the increasing amount of the generated  $H_2$  bubbles.<sup>68</sup> Yet, on the other hand, the synergy between Pt and  $MoS_2$  should be enhanced. This is because the total number of the active sites increases with the Pt loading, signified by the decreasing onset potential as a function of the Pt content (Figure 7a) and the increasing HER performance (Figure 6a,b). At low overpotential of  $-0.1$  V vs RHE, the Pt– $MoS_2$  synergy is only activated with the highest Pt loading, verified by the increased hydrogen evolution rate beyond the critical overpotential (olive dashed line in Figure 6a). The synergistic behavior in the 5 wt % Pt: $MoS_2$  dendrites is dominant over the agglomeration of Pt, and therefore the current density exhibits a superlinear trend with the Pt loading (Figure 7d). Since at high overpotential of  $-0.3$  V vs RHE, the synergies are switched on for both 1 wt % and 5 wt % Pt loadings (navy and olive dashed lines in Figure 6a, respectively), the impacts of the Pt size would surpass that of the Pt– $MoS_2$  synergy, leading to a sublinear relationship (Figure 7f). These competing mechanisms turn out to deliver an apparent linear curve at  $-0.2$  V vs RHE (Figure 7e).

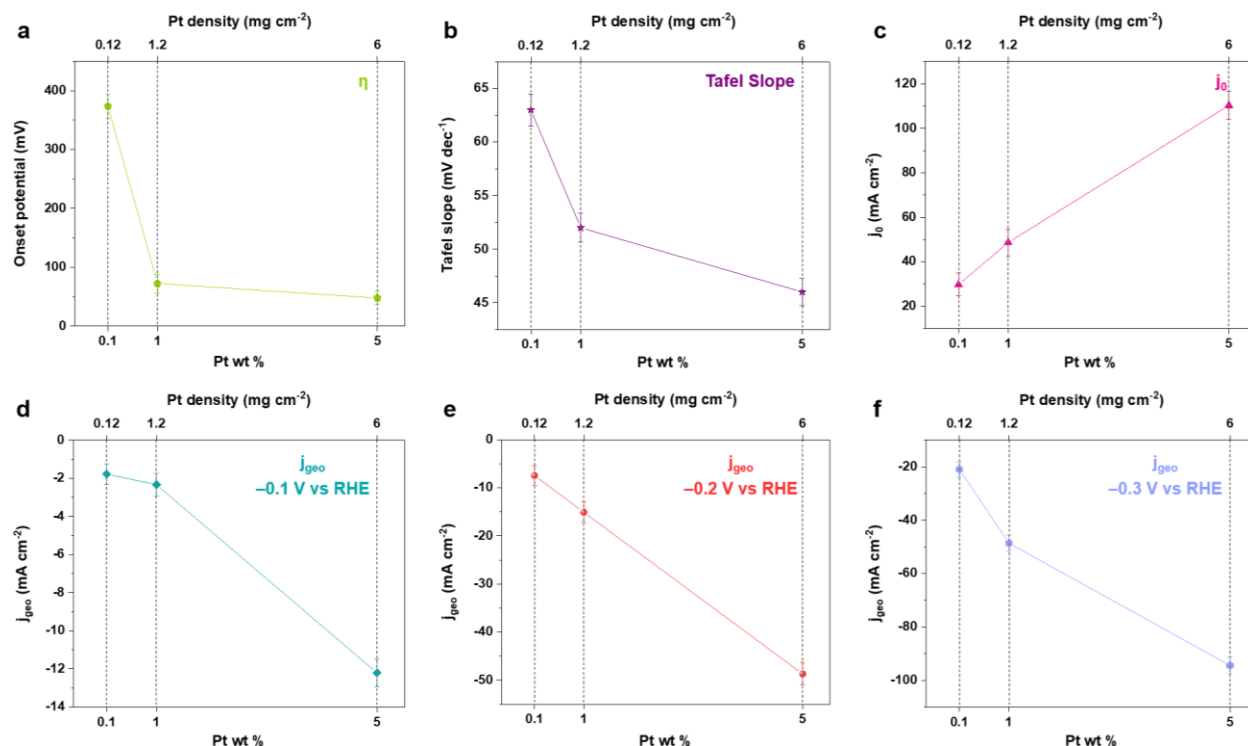


**Figure 7.** Pt content dependence of the HER activities in Pt:MoS<sub>2</sub> dendrite hybrids, with regards to the (a)  $\eta$ , (b) Tafel slope, (c)  $j_0$ , current density at (d)  $-0.1$  V, (e)  $-0.2$  V, and (f)  $-0.3$  V vs RHE. The deviations from averaged values could stem from the areal coverage fluctuations of the dendrites.

**Conductivity.** The electrical conductivity of the catalyst system is measured by electrochemical impedance spectroscopy (EIS), Figure 6c. Within the frequency range of 200 000 to 1 Hz, the semiarc at low frequency region indicates the kinetic control in the electrode process. Mass transport control is excluded, otherwise a 45° straight line would be shown. The absence of another semiarc at high frequency region is due to the decreased electron tunneling barrier between the directly grown catalyst layer and the GC electrode compared to that for the MoS<sub>2</sub> transferred on it.<sup>10,19,69</sup> The better interfacial contact accounting for this benefits from the direct growth on the electrode and the thermal annealing treatment. Also, the  $x$ -axis intercept represents the ohmic impedance of the electrochemical reaction system.<sup>70</sup> The smaller semiarc radius and smaller  $x$ -



intercept reveal the lower charge transfer resistance ( $R_{ct}$ ) at the hybrid–electrolyte interface and the lower series resistance ( $R_s$ ) of the cocatalyst, respectively, which is attributable to both the metallicity of Pt and the dendritic morphology (containing more electron hopping sites) of MoS<sub>2</sub>.

**Durability.** To simulate the realistic operation of water-splitting devices, our dendritic monolayer Pt:MoS<sub>2</sub> cocatalysts have been subjected to durability tests through LSV at a fast scan rate of 100 mV s<sup>-1</sup> in the same aqueous environment (0.5 M H<sub>2</sub>SO<sub>4</sub>) for the HER. The Pt:MoS<sub>2</sub> hybrid untreated with annealing exhibits low stability upon cycling (Figure 6d). The degradation is likely to stem from the behavior of Pt nanoclusters as follows:<sup>68</sup> (1) Ostwald ripening, by which small metal crystals dissolve and then redeposit onto larger crystals. (2) Aggregation, occurring when the Pt particles migrate across the surfaces of MoS<sub>2</sub> as well as the GC plate via Brownian motion. Both (1) and (2) would cause Pt sintering with a reduction in the active surface area, and thereby hampering its electrocatalysis and stability. (3) Detachment from the GC electrode, as the Pt nanoclusters could be prone to subtle disturbance in fluids. To mechanistically understand the degradation, we have probed the chemical bonding (Pt–MoS<sub>2</sub>) and physical adhesion (Pt:MoS<sub>2</sub> hybrids to GC electrode) by XPS (Figure S9) and SEM imaging (Figure 6f,g), in conjunction with the electrochemical measurements (Figure 6d,e). For the non-annealed sample, the SEM image indicates the cycling-induced loss of both Pt and MoS<sub>2</sub> (Figure 6f). This is supported by the increase in  $\eta$  (Figure 6d), reflects the altered catalytic sites, as well as the intensity quenching of Mo 3d, S 2p, and Pt 4f peaks in the XPS spectra (Figure S9). The Mo 3d and S 2p peaks shift farther away from those of pristine MoS<sub>2</sub>, and the Pt 4f peaks shift towards Pt<sup>δ+</sup>, signifying that a higher percentage of the preserved Pt is chemically bound to the MoS<sub>2</sub>, and the detached Pt is more likely to have been physically adsorbed on the MoS<sub>2</sub>. The increased percentage of the S-bound Pt after cycling is also verified by the larger position differences between the Pt 4f peaks along with

the smaller position differences between the S 2p peaks (Table S2). The Mo 3d peaks are red-shifted due to the n-doping induced by the binding of its nearest neighboring S to Pt, while the position difference between them stays unchanged, implicating again the absence of Pt–Mo bonds in our system. Notably, if Ostwald ripening and aggregation of the Pt occur before detachment, the Pt 4f peaks might shift intermediately towards Pt<sup>0</sup> because of the weakened chemisorption to the MoS<sub>2</sub>. But these are not the eventually dominant causes for the deteriorated HER performance over the materials loss.

Aiming to enhance physisorption of the hybrid to the electrode surface and obtain durable catalysts for the HER, we have involved a thermal annealing stage in the APCVD process (Figure 1c). The HER activities of the 5 wt % Pt:MoS<sub>2</sub> dendrite hybrid annealed under the optimized conditions is stable after 3,000 cycles (350–600 °C for 25 min). Increasing the temperature can enhance the physical adsorption between Pt and its MoS<sub>2</sub> scaffold,<sup>71</sup> whereas this would reduce the free energies of Ostwald ripening and aggregation. Therefore, the aforementioned three processes should compete against one another at an elevated temperature, assuming that more than one would happen. The stronger physisorption at the Pt–MoS<sub>2</sub> interface plays a predominant role within this temperature range over the facilitated Ostwald ripening and aggregation of Pt nanocrystals, aside from the enhanced chemisorption of Mo-edges to the GC support, which might exist and could lead to weaker hydrogen binding.<sup>72</sup> Lower temperature cannot guarantee the sufficient adhesion enhancement (Figure 6d), and further increasing the temperature above 600 °C would cause the decomposition of MoS<sub>2</sub>.<sup>41</sup> The improved long-term stability (~12 h) is validated by chronoamperometry (Figure 6e) and SEM imaging (Figure 6g).<sup>42</sup> We have not seen changes in the XPS spectra before and after annealing, which means that the chemisorption between Pt and

MoS<sub>2</sub> is unaffected during this treatment. The reason is that the annealing temperature is much lower than that of the main growth where most chemical bonds are formed.

**Outperformance of Dendrite.** The dendritic MoS<sub>2</sub> scaffold is advantageous over the triangular counterpart in three aspects. (1) Higher densities of catalytic centers: the dendrite surface is enriched with S defects and undercoordinated Mo atoms. Both of these sites exhibit HER activities.<sup>5,14,25,64,65</sup> (2) Preferences of Pt seeding: at reduced Pt density, the edges and defects are the energetically more favorable sites compared with the lattice plane to stabilize the Pt.<sup>7,30,32,33</sup> Besides, the dendrites possess a 23% larger surface area than the triangles, as indicated by the SEM images in Figure 2b and Figure S2. This would allow more Pt atoms to be bound on the MoS<sub>2</sub> and enable more interactions between them. (3) Increased conductivity: the higher densities of exposed edges and defects can bring more pairing chances of the hopping e<sup>-</sup> on the electrode and the H<sub>3</sub>O<sup>+</sup> in the electrolyte to form chemisorbed H\*, and the promoted Pt stabilization can reduce the ohmic impedance of the reaction system, which are evidenced by its lower  $R_{ct}$  and  $R_s$  (Figure 6c), respectively. Based on these, the advantages of dendrite are embodied in both the hydrogen evolution catalysis of Pt and MoS<sub>2</sub> themselves and the synergies in this cocatalyst system (Figure S8). The enhanced synergies in our dendritic-shaped hybrids can be confirmed by assessing the kinetic parameters for the HER: (1) the value differences between 0.1 wt % Pt:MoS<sub>2</sub> dendrites and pristine MoS<sub>2</sub> dendrites are larger than those between 0.1 wt % Pt:MoS<sub>2</sub> triangles and pristine MoS<sub>2</sub> triangles; (2) the value differences between 0.1 wt % Pt:MoS<sub>2</sub> dendrites and 0.1 wt % Pt:MoS<sub>2</sub> triangles are larger than those between pristine MoS<sub>2</sub> dendrites and pristine MoS<sub>2</sub> triangles; (3) the  $j_0$  of 0.1 wt % Pt:MoS<sub>2</sub> dendrites is higher than the sum of that of pristine MoS<sub>2</sub> dendrites and 0.1 wt % Pt:MoS<sub>2</sub> triangles. The increment in  $j_0$  reveals that the electron transfer is accelerated by employing MoS<sub>2</sub> dendrites to accommodate the Pt. As a consequence, the rates of

the Volmer and Heyrovsky reactions are both increased, leading to an enhancement in the HER efficiency.

**Table 1.** Key parameters for HER of the pristine and Pt-loaded MoS<sub>2</sub> monolayer domains in this study.

The averages are taken from 4 samples

	Onset potential $\eta$ (mV)	Tafel slope (mV dec <sup>-1</sup> )	Exchange current density $j_0$ ( $\mu\text{A cm}^{-2}$ )
Pristine MoS <sub>2</sub> triangles	525 $\pm$ 34.8	127 $\pm$ 3.9	0.7 $\pm$ 0.1
Pristine MoS <sub>2</sub> dendrites	487 $\pm$ 29.6	112 $\pm$ 3.5	18.5 $\pm$ 2.0
0.1 wt % Pt:MoS <sub>2</sub> triangles	419 $\pm$ 27.1	90 $\pm$ 3.0	4.2 $\pm$ 0.3
0.1 wt % Pt:MoS <sub>2</sub> dendrites	374 $\pm$ 20.7	63 $\pm$ 1.5	29.7 $\pm$ 5.1
1 wt % Pt:MoS <sub>2</sub> dendrites	72 $\pm$ 16.3	52 $\pm$ 1.4	48.6 $\pm$ 6.2
5 wt % Pt:MoS <sub>2</sub> dendrites	48 $\pm$ 11.2	46 $\pm$ 1.3	110.3 $\pm$ 6.4

**Comparisons with Literature.** The key HER electrocatalytic parameters of the low-dimensional Pt:MoS<sub>2</sub> reported to date are summarized in Table S3. There are variations in the materials interactions, morphologies, defect and strain states, synthetic approaches, etc. We have been dedicated to developing a single-step approach to produce directly applicable catalysts, improving the HER performance, increasing the stability, and discovering the catalytic mechanism including the synergistic effects in our unique system. Comparative analysis regarding the HER performance outlines five reasons for the high density of catalytic sites on the dendrite hybrids in the present study vs the previously reported Pt:MoS<sub>2</sub> with similar doping percentages.<sup>43</sup> (1) The monolayer thickness of the MoS<sub>2</sub> that we have grown leads to decreased potential barrier for electron hopping within the interlayer gap and hence increased efficiency of charge transfer from the electrode,<sup>35</sup> consequently facilitating the hydrogen evolution process. (2) The dendritic scaffold

contains plenty of edges and grain boundaries, both of which intrinsically exhibit electrocatalysis for the HER. (3) These featured sites could show higher adsorption energy for the Pt species,<sup>7,33</sup> so that the Pt is more easily seeded and stabilized on the dendritic MoS<sub>2</sub>. (4) Enhanced synergistic effects between Pt and MoS<sub>2</sub> are achieved owing to the improvement in Pt density and bonding strength.<sup>7,42,62,63</sup> (5) Synergy also emerges among the highly dispersed Pt species. This is attributed to the short separation distances between small Pt nanoclusters and single Pt atoms, which result in increased electron channels (hence conductivity) and Pt specific surface area (hence utilization ratio).<sup>61</sup> Overall, the improved HER activities of our dendrite hybrids mainly benefit from the morphology design of the MoS<sub>2</sub> and Pt.

## CONCLUSION

In summary, Pt:MoS<sub>2</sub> cocatalyst systems have been constructed utilizing single-step APCVD approach. We have determined the loading threshold for producing Pt:MoS<sub>2</sub> hybrids against Pt:Mo alloys. The growth mode has been controlled to be either thermodynamic or kinetic, yielding either triangular or dendritic structures. The Pt shows high dispersion on the monolayer MoS<sub>2</sub> as surface-bound single atoms and small nanocrystals. The enriched edges and defects of dendritic-shaped MoS<sub>2</sub> show HER activities and are the preferential sites for stabilizing the Pt via chemical binding. These endow the Pt:MoS<sub>2</sub> dendrite with a greatly higher density of electrocatalytically active sites both at its edges and on its surface covering a large area up to sub-cm scale. In addition, the monolayer thickness and the dendritic morphology lead to rapid charge transfer and low resistance. The Pt and MoS<sub>2</sub> not only engage in the catalysis individually, but also have synergistic effects, i.e., the Pt–S bonds improve the HER behavior of Mo at the edges and create more catalytic sites on the surface. The rate-limiting step in the HER is thereby regulated from Volmer towards

Heyrovsky route, demonstrating the interactive impacts of MoS<sub>2</sub> shape engineering and its hybridization with Pt on achieving increased hydrogen evolution efficiency. By demonstrating the direct synthesis of 2D nanocatalysts with reasonable performance, good conductivity, and high durability, we have paved a feasible avenue for practical application in water electrolysis.

## EXPERIMENTAL SECTION

**APCVD Synthesis of Pt:MoS<sub>2</sub> Hybrid.** The Pt:MoS<sub>2</sub> hybrids were grown by APCVD using molybdenum trioxide (MoO<sub>3</sub>, powder, ≥99.5%, Sigma-Aldrich) and sulfur (S, powder, ≥99.5%, Sigma-Aldrich) as the precursors. Chloroplatinic acid hydrate (H<sub>2</sub>PtCl<sub>6</sub> · xH<sub>2</sub>O, 99.995%, Sigma-Aldrich) was the Pt source. The growth substrate, conductive GC thin plate (2 cm × 1.5 cm), was sonicated for 10 min in acetone and isopropanol solution successively. The H<sub>2</sub>PtCl<sub>6</sub> · xH<sub>2</sub>O was dehydrated at 220 °C under vacuum for ~2 h. The PtCl<sub>4</sub> product was dissolved into acetone and dispersed by sonication to prepare 0.01 M solution, which were then drop-casted onto the GC substrate surface through μL burette and carefully applied with cotton bud. We employed double-walled quartz tubes for the synthesis to avoid cross-reaction between the reactants of MoO<sub>3</sub> and S. Two separate furnaces were utilized for individual temperature control. The MoO<sub>3</sub> (15 mg) put in the inner tube (0.6 inch diameter) was positioned in the central zone of the low-temperature furnace, and the S (600 mg) put in the outer tube (1 inch diameter) was positioned 1.7 cm from the left open end of the high-temperature furnace. The GC plate was located downstream at the center of the high-temperature furnace (Figure 1b). To produce triangular domains, the GC substrate was placed near the medial axis of the outer tube, where the Mo:S ratio was ~1:2 during the synthesis, resulting in thermodynamic growth. To produce dendritic domains, the GC substrate was placed in close proximity to the wall of the outer tube, where the Mo:S ratio was <<1:2, deriving kinetic

growth.<sup>36,71</sup> After driving off the oxygen and moisture by flushing the reaction system with 500 sccm argon (Ar) for 30 min, the low- and high-temperature furnaces were ramped up to ~180 and ~200 °C, respectively, whereby a sulfur-rich environment was created. The vaporous precursors were transported to the GC substrate surface by the carrier gases of argon (Ar) and hydrogen (H<sub>2</sub>).

(1) Nucleation. The high-temperature furnace was heated up to 800 °C. The temperature of MoO<sub>3</sub> was raised to 300 °C in the meanwhile. Once the target temperature was reached, the MoS<sub>2</sub> began to nucleate with 150 sccm Ar flow and 10 sccm H<sub>2</sub> flow. Plenty of nuclei could be formed within 20 min. (2) Main growth. This stage lasted for 25 min, with the Ar flow rate decreased to 50 sccm. (3) Edge attachment. We devised this 15 min process in order to get highly uniform monolayer structures and increase the domain size, which was realized by allowing the atoms to migrate freely across the surfaces of GC and MoS<sub>2</sub> before attaching to the more thermodynamically favorable edges. The Ar and H<sub>2</sub> flow rates were respectively dropped to 5 and 0 sccm for lower precursor feedstocks. The GC temperature was decreased to 700 °C so as to attenuate the sublimation of MoS<sub>2</sub> that had been synthesized on the substrate. The MoO<sub>3</sub> temperature was reduced to 270 °C, in which way the production of dendrites following a DLA-like process could be guaranteed by the declined Mo:S ratio. The temperature of S slowly climbed from 180 °C to 200 °C during (2) and (3) to maintain the S vapor concentration at a nearly constant level. (4) Thermal annealing. As soon as the synthesis was finished, we annealed the sample in situ at 350 °C for 25 min, leading to enhanced physical adhesions of both the Pt:MoS<sub>2</sub> hybrid to the GC support. Finally, it ended up with fast cooling.

**Characterization.** The samples were imaged at room temperature utilizing optical microscope, scanning electron microscope (SEM, Hitachi-4300, 3.0 kV accelerating voltage), and ADF-STEM (JEOL ARM-200F STEM) with a CEOS aberration corrector, 80 kV accelerating voltage). Dwell

times of 32  $\mu$ s and a pixel size of 0.0073–0.015 nm px<sup>-1</sup> were applied for the ADF-STEM imaging, along with a 30  $\mu$ m CL aperture, 24.6 mrad convergence semiangle, 12 pA beam current, and 39–156 mrad inner acquisition angle. The ADF-STEM images were subjected to a Gaussian smooth. The Raman and PL spectra were recorded with a JY Horiba LabRAM ARAMIS imaging confocal Raman microscope. The domain was excited by a 12.5 mW, 532 nm (2.33 eV) diode laser, which was focused down to a  $\sim$ 1  $\mu$ m spot. The acquisition times for spectra and maps were 1 and 0.1 s, respectively. AFM was used to measure the layer thickness by Asylum Research MFP-3D in AC mode with a silicon AC-160TS cantilever (Olympus, spring constant of  $\sim$ 42 N m<sup>-1</sup> and resonant frequency of  $\sim$ 300 kHz). As for the XPS, the samples were examined using a Thermo Scientific K-Alpha instrument equipped with a microfocused monochromated Al X-ray source, which was operated at 12 keV. The diameter of the spot was 400  $\mu$ m and the detection depth was 10 nm. The analyzer operates at a constant analyzer energy (CAE) of 200 eV for survey scans and 50 eV for detailed scans. The charges were neutralized by a combined low energy/ion flood source. Data acquisition and analysis were performed with Thermo Scientific Advantage and CasaXPS software, respectively.

**Electrochemical Measurements.** The catalytic performance was tested in a three-electrode system, using the Pt:MoS<sub>2</sub> or pristine MoS<sub>2</sub> grown on the GC as the working electrode, a carbon rod as the counter electrode, and Ag/AgCl/KCl (3 M) as the reference electrode. A defined working area of the sample was immersed into a 0.5 M H<sub>2</sub>SO<sub>4</sub> N<sub>2</sub>-purged solution for HER activities. The potentials were calibrated to a reversible hydrogen electrode, i.e.,  $E(\text{RHE}) = E(\text{Ag/AgCl/KCl (3 M)}) + 0.21 - 0.059 \text{ pH}$ . The LSV was conducted under quasi-equilibrium conditions at 1 mV s<sup>-1</sup>, whereas the cyclic voltammetry (CV) was applied at a fast scan rate of 100 mV s<sup>-1</sup>. EIS was



measured by sweeping the frequency from 200 000 to 1 Hz with a perturbation voltage amplitude of 10 mV. The chronoamperometry was carried out at the overpotential of  $-0.2$  V vs RHE.

### Supporting Information

Edges and grain boundaries of pristine MoS<sub>2</sub> dendrites, Pt loading on monolayer MoS<sub>2</sub> triangles, effects of heavy Pt loading on APCVD, elemental composition and chemical states in Pt:Mo alloys, ADF-STEM images of the Pt on monolayer MoS<sub>2</sub>, wide-range Tafel plots, individual and synergistic effects of Pt and MoS<sub>2</sub> on the HER, XPS measurements of the degraded and stabilized Pt:MoS<sub>2</sub> dendrites, HER performances of the Pt-decorated MoS<sub>2</sub> reported to date

### ACKNOWLEDGMENTS

J.H.W. thanks The University of Texas at Austin for support.

### REFERENCES

- (1) Norskov, J. K.; Christensen, Claus H. Toward Efficient Hydrogen Production at Surfaces. *Science* **2006**, *312*, 1322–1323.
- (2) Morales-Guio, C. G.; Stern, L.-A.; Hu, X. Nanostructured Hydrotreating Catalysts for Electrochemical Hydrogen Evolution. *Chem. Soc. Rev.* **2014**, *43*, 6555–6569.
- (3) Benck J. D.; Hellstern, T. R.; Kibsgaard, J.; Chakthranont, P.; Jaramillo, T. F. Catalyzing the Hydrogen Evolution Reaction (HER) with Molybdenum Sulfide Nanomaterials. *ACS Catal.* **2014**, *4*, 3957–3971.
- (4) Hinnemann, B.; Moses, P. G.; Bonde, J.; Jørgensen, K. P.; Nielsen, J. H.; Horch, S.; Chorkendorff, I.; Nørskov, J. K. Biomimetic Hydrogen Evolution: MoS<sub>2</sub> Nanoparticles as

- Catalyst for Hydrogen Evolution. *J. Am. Chem. Soc.* **2005**, *127*, 5308–5309.
- (5) Jaramillo, T. F.; Jørgensen, K. P.; Bonde, J.; Nielsen, J. H.; Horch, S.; Chorkendorff, I. Identification of Active Edge Sites for Electrochemical H<sub>2</sub> Evolution from MoS<sub>2</sub> Nanocatalysts. *Science* **2007**, *317*, 100–102.
- (6) Yang, Y.; Fei, H.; Ruan, G.; Xiang, C.; Tour, J. M. Edge-Oriented MoS<sub>2</sub> Nanoporous Films as Flexible Electrodes for Hydrogen Evolution Reactions and Supercapacitor Devices. *Adv. Mater.* **2014**, *26*, 8163–8168.
- (7) Li, S.; Lee, J. K.; Zhou, S.; Pasta, M.; Warner, J. H. Synthesis of Surface Grown Pt Nanoparticles on Edge-Enriched MoS<sub>2</sub> Porous Thin Films for Enhancing Electrochemical Performance. *Chem. Mater.* **2019**, *31*, 387–397.
- (8) Kong, D.; Wang, H.; Cha, J. J.; Pasta, M.; Koski, K. J.; Yao, J.; Cui, Y. Synthesis of MoS<sub>2</sub> and MoSe<sub>2</sub> Films with Vertically Aligned Layers. *Nano Lett.* **2013**, *13*, 1341–1347.
- (9) Li, S.; Wang, S.; Salamone, M. M.; Robertson, A. W.; Nayak, S.; Kim, H.; Tsang, S. C. E.; Pasta, M.; Warner, J. H. Edge-Enriched 2D MoS<sub>2</sub> Thin Films Grown by Chemical Vapor Deposition for Enhanced Catalytic Performance. *ACS Catal.* **2017**, *7*, 877–886.
- (10) Xu, W.; Li, S.; Zhou, S.; Lee, J. K.; Wang, S.; Sarwat, S. G.; Wang, X.; Bhaskaran, H.; Pasta, M.; Warner, J. H. Large Dendritic Monolayer MoS<sub>2</sub> Grown by Atmospheric Pressure Chemical Vapor Deposition for Electrocatalysis. *ACS Appl. Mater. Interfaces* **2018**, *10*, 4630–4639.
- (11) Sun, Y.; Alimohammadi, F.; Zhang, D.; Guo, G. Enabling Colloidal Synthesis of Edge-Oriented MoS<sub>2</sub> with Expanded Interlayer Spacing for Enhanced HER Catalysis. *Nano Lett.* **2017**, *17*, 1963–1969.
- (12) Lukowski, M. A.; Daniel, A. S.; Meng, F.; Forticaux, A.; Li, L.; Jin, S. Enhanced Hydrogen

- Evolution Catalysis from Chemically Exfoliated Metallic MoS<sub>2</sub> Nanosheets. *J. Am. Chem. Soc.* **2013**, *135*, 10274–10277.
- (13) Voiry, D.; Salehi, M.; Silva, R.; Fujita, T.; Chen, M.; Asefa, T.; Shenoy, V. B.; Eda, G.; Chhowalla, M. Conducting MoS<sub>2</sub> Nanosheets as Catalysts for Hydrogen Evolution Reaction. *Nano Lett.* **2013**, *13*, 6222–6227.
- (14) Yin, Y.; Han, J.; Zhang, Y.; Zhang, X.; Xu, P.; Yuan, Q.; Samad, L.; Wang, X.; Wang, Y.; Zhang, Z.; Zhang, P.; Cao, X.; Song, B.; Jin, S. Contributions of Phase, Sulfur Vacancies, and Edges to the Hydrogen Evolution Reaction Catalytic Activity of Porous Molybdenum Disulfide Nanosheets. *J. Am. Chem. Soc.* **2016**, *138*, 7965–7972.
- (15) Li, H.; Tsai, C.; Koh, A. L.; Cai, L.; Contryman, A. W.; Fragapane, A. H.; Zhao, J.; Han, H. S.; Manoharan, H. C.; Abild-Pedersen, F.; Nørskov, J. K.; Zheng, X. Activating and Optimizing MoS<sub>2</sub> Basal Planes for Hydrogen Evolution through the Formation of Strained Sulphur Vacancies. *Nat. Mater.* **2016**, *15*, 48–53.
- (16) Ye, G.; Gong, Y.; Lin, J.; Li, B.; He, Y.; Pantelides, S. T.; Zhou, W.; Vajtai, R.; Ajayan, P. M. Defects Engineered Monolayer MoS<sub>2</sub> for Improved Hydrogen Evolution Reaction. *Nano Lett.* **2016**, *16*, 1097–1103.
- (17) Huang, N.; Peng, R.; Ding, Y.; Yan, S.; Li, G.; Sun, P.; Sun, X.; Liu, X.; Yu, H. Facile Chemical-Vapour-Deposition Synthesis of Vertically Aligned Co-Doped MoS<sub>2</sub> Nanosheets as an Efficient Catalyst for Triiodide Reduction and Hydrogen Evolution Reaction. *J. Catal.* **2019**, *373*, 250–259.
- (18) Wang, Y.; Udyavara, S.; Neurock, M.; Frisbie, C. D. Field Effect Modulation of Electrocatalytic Hydrogen Evolution at Back-Gated Two-Dimensional MoS<sub>2</sub> Electrodes. *Nano Lett.* **2019**, *19*, 6118–6123.

- (19) Li, G.; Chen, Z.; Li, Y.; Zhang, D.; Yang, W.; Liu, Y.; Cao, L. Engineering Substrate Interaction to Improve Hydrogen Evolution Catalysis of Monolayer MoS<sub>2</sub> Films Beyond Pt. *ACS Nano* **2020**, *14*, 1707–1714.
- (20) Zheng, X.; Xu, J.; Yan, K.; Wang, H.; Wang, Z.; Yang, S. Space-Confined Growth of MoS<sub>2</sub> Nanosheets within Graphite: The Layered Hybrid of MoS<sub>2</sub> and Graphene as an Active Catalyst for Hydrogen Evolution Reaction. *Chem. Mater.* **2014**, *26*, 2344–2353.
- (21) Gao, M.-R.; Liang, J.-X.; Zheng, Y.-R.; Xu, Y.-F.; Jiang, J.; Gao, Q.; Li, J.; Yu, S.-H. An Efficient Molybdenum Disulfide/Cobalt Diselenide Hybrid Catalyst for Electrochemical Hydrogen Generation. *Nat. Commun.* **2015**, *6*, 5982.
- (22) Zuo, P.; Jiang, L.; Li, X.; Li, B.; Ran, P.; Li, X.; Qu, L.; Lu, Y. Metal (Ag, Pt)–MoS<sub>2</sub> Hybrids Greenly Prepared Through Photochemical Reduction of Femtosecond Laser Pulses for SERS and HER. *ACS Sustainable Chem. Eng.* **2018**, *6*, 7704–7714.
- (23) Xu, Q.; Liu, Y.; Jiang, H.; Hu, Y.; Liu, H.; Li, C. Unsaturated Sulfur Edge Engineering of Strongly Coupled MoS<sub>2</sub> Nanosheet–Carbon Macroporous Hybrid Catalyst for Enhanced Hydrogen Generation. *Adv. Energy Mater.* **2019**, *9*, 1802553.
- (24) Zhou, Y.; Pondick, J. V.; Silva, J. L.; Woods, J. M.; Hynek, D. J.; Matthews, G.; Shen, X.; Feng, Q.; Liu, W.; Lu, Z.; Liang, Z.; Brena, B.; Cai, Z.; Wu, M.; Jiao, L.; Hu, S.; Wang, H.; Araujo, C. M.; Cha, J. J. Unveiling the Interfacial Effects for Enhanced Hydrogen Evolution Reaction on MoS<sub>2</sub>/WTe<sub>2</sub> Hybrid Structures. *Small*, **2019**, *15*, 1900078.
- (25) Li, G.; Zhang, D.; Qiao, Q.; Yu, Y.; Peterson, D.; Zafar, A.; Kumar, R.; Curtarolo, S.; Hunte, F.; Shannon, S.; Zhu, Y.; Yang, W.; Cao, L. All the Catalytic Active Sites of MoS<sub>2</sub> for Hydrogen Evolution. *J. Am. Chem. Soc.* **2016**, *138*, 16632–16638.
- (26) Deng, J.; Li, H.; Xiao, J.; Tu, Y.; Deng, D.; Yang, H.; Tian, H.; Li, J.; Ren, P.; Bao, X.

- Triggering the Electrocatalytic Hydrogen Evolution Activity of the Inert Two-Dimensional MoS<sub>2</sub> Surface via Single-Atom Metal Doping. *Energy Environ. Sci.* **2015**, *8*, 1594–1601.
- (27) Yuwen, L.; Xu, F.; Xue, B.; Luo, Z.; Zhang, Q.; Bao, B.; Su, S.; Weng, L.; Huang, W.; Wang, L. General Synthesis of Noble Metal (Au, Ag, Pd, Pt) Nanocrystal Modified MoS<sub>2</sub> Nanosheets and the Enhanced Catalytic Activity of Pd–MoS<sub>2</sub> for Methanol Oxidation. *Nanoscale* **2014**, *6*, 5762–5769.
- (28) Ying, J.; Jiang, G.; Paul Cano, Z.; Han, L.; Yang, X. Y.; Chen, Z. Nitrogen-Doped Hollow Porous Carbon Polyhedrons Embedded with Highly Dispersed Pt Nanoparticles as a Highly Efficient and Stable Hydrogen Evolution Electrocatalyst. *Nano Energy* **2017**, *40*, 88–94.
- (29) Deng, D.; Novoselov, K. S.; Fu, Q.; Zheng, N.; Tian, Z.; Bao, X. Catalysis with Two-Dimensional Materials and Their Heterostructures. *Nat. Nanotechnol.* **2016**, *11*, 218–230.
- (30) Li, H.; Wang, S.; Sawada, H.; Han, G. G. D.; Samuels, T.; Allen, C. S.; Kirkland, A. I.; Grossman, J. C.; Warner, J. H. Atomic Structure and Dynamics of Single Platinum Atom Interactions with Monolayer MoS<sub>2</sub>. *ACS Nano* **2017**, *11*, 3392–3403.
- (31) Li, H.; Du, M.; Mleczko, M. J.; Koh, A. L.; Nishi, Y.; Pop, E.; Bard, A. J.; Zheng, X. Kinetic Study of Hydrogen Evolution Reaction over Strained MoS<sub>2</sub> with Sulfur Vacancies Using Scanning Electrochemical Microscopy. *J. Am. Chem. Soc.* **2016**, *138*, 5123–5129.
- (32) Xie, J.; Gao, L.; Jiang, H.; Zhang, X.; Lei, F.; Hao, P.; Tang, B.; Xie, Y. Platinum Nanocrystals Decorated on Defect-Rich MoS<sub>2</sub> Nanosheets for pH-Universal Hydrogen Evolution Reaction. *Cryst. Growth Des.* **2019**, *19*, 60–65.
- (33) Wang, S.; Sawada, H.; Han, X.; Zhou, S.; Li, S.; Guo, Z. X.; Kirkland, A. I.; Warner, J. H. Preferential Pt Nanocluster Seeding at Grain Boundary Dislocations in Polycrystalline Monolayer MoS<sub>2</sub>. *ACS Nano* **2018**, *12*, 5626–5636.

- (34) Zhang, Y.; Ji, Q.; Wen, J.; Li, J.; Li, C.; Shi, J.; Zhou, X.; Shi, K.; Chen, H.; Li, Y.; Deng, S.; Xu, N.; Liu, Z.; Zhang, Y. Monolayer MoS<sub>2</sub> Dendrites on a Symmetry-Disparate SrTiO<sub>3</sub> (001) Substrate: Formation Mechanism and Interface Interaction. *Adv. Funct. Mater.* **2016**, *26*, 3299–3305.
- (35) Yu, Y.; Huang, S.-Y.; Li, Y.; Steinmann, S. N.; Yang, W.; Cao, L. Layer-Dependent Electrocatalysis of MoS<sub>2</sub> for Hydrogen Evolution. *Nano Lett.* **2014**, *14*, 553–558.
- (36) Wang, J.; Cai, X.; Shi, R.; Wu, Z.; Wang, W.; Long, G.; Tang, Y.; Cai, N.; Ouyang, W.; Geng, P.; Chandrashekar, B. N.; Amini, A.; Wang, N.; Cheng, C. Twin Defect Derived Growth of Atomically Thin MoS<sub>2</sub> Dendrites. *ACS Nano* **2017**, *12*, 635–643.
- (37) Zhang, K.; Feng, S.; Wang, J.; Azcatl, A.; Lu, N.; Addou, R.; Wang, N.; Zhou, C.; Lerach, J.; Bojan, V.; Kim, M. J.; Chen, L.-Q.; Wallace, R. M.; Terrones, M.; Zhu, J.; Robinson, J. A. Manganese Doping of Monolayer MoS<sub>2</sub>: The Substrate Is Critical. *Nano Lett.* **2015**, *15*, 6586–6591.
- (38) Splendiani, A.; Sun, L.; Zhang, Y.; Li, T.; Kim, J.; Chim, C.-Y.; Galli, G.; Wang, F. Emerging Photoluminescence in Monolayer MoS<sub>2</sub>. *Nano Lett.* **2010**, *10*, 1271–1275.
- (39) Stojić, D. L.; Grozdić, T. D.; Kaninski, M. P. M.; Stanić, V. Đ. Electrocatalytic Effects of Mo–Pt Intermetallics Singly and with Ionic Activators. Hydrogen Production via Electrolysis. *Int. J. Hydrogen Energy* **2007**, *32*, 2314–2319.
- (40) Ren, W.; Zhang, H.; Cheng, C. Ultrafine Pt Nanoparticles Decorated MoS<sub>2</sub> Nanosheets with Significantly Improved Hydrogen Evolution Activity. *Electrochim. Acta* **2017**, *241*, 316–322.
- (41) Chen, P.; Xu, W.; Gao, Y.; Holdway, P.; Warner, J. H.; Castell, M. R. Thermal Degradation of Monolayer MoS<sub>2</sub> on SrTiO<sub>3</sub> Supports. *J. Phys. Chem. C* **2019**, *123*, 3876–3885.

- (42) Hou, D.; Zhou, W.; Liu, X.; Zhou, K.; Xie, J.; Li, G.; Chen, S. Pt Nanoparticles/MoS<sub>2</sub> Nanosheets/Carbon Fibers as Efficient Catalyst for the Hydrogen Evolution Reaction. *Electrochim. Acta* **2015**, *166*, 26–31.
- (43) Wu, C.; Li, D.; Ding, S.; Rehman, Z. U.; Liu, Q.; Chen, S.; Zhang, B.; Song, Li. Monoatomic Platinum-Anchored Metallic MoS<sub>2</sub>: Correlation between Surface Dopant and Hydrogen Evolution. *J. Phys. Chem. Lett.* **2019**, *10*, 6081–6087.
- (44) Saidi, W. A. Density Functional Theory Study of Nucleation and Growth of Pt Nanoparticles on MoS<sub>2</sub>(001) Surface. *Cryst. Growth Des.* **2015**, *15*, 642–652.
- (45) Saidi, W. A. Trends in the Adsorption and Growth Morphology of Metals on the MoS<sub>2</sub>(001) Surface. *Cryst. Growth Des.* **2015**, *15*, 3190–3200.
- (46) Shi, Y.; Song, B.; Shahbazian-Yassar, R.; Zhao, J.; Saidi, W. A. Experimentally Validated Structures of Supported Metal Nanoclusters on MoS<sub>2</sub>. *J. Phys. Chem. Lett.* **2018**, *9*, 2972–2978.
- (47) Gao, J.; Zou, J.; Zeng, X.; Ding, W. Carbon Supported Nano Pt–Mo Alloy Catalysts for Oxygen Reduction in Magnesium–Air Batteries. *RSC Adv.* **2016**, *6*, 83025–83030.
- (48) Wang, J.; Cao, X.; Fang, L.; You, X.; Wong, K.; Cao, S.; Xiao, C.; Cai, S.; Huang, Y.; Zhang, X.; Chen, Z. MoS<sub>2</sub> Nanoflower Supported Pt Nanoparticle as an Efficient Electrocatalyst for Ethanol Oxidation Reaction. *Int. J. Hydrogen Energy* **2019**, *44*, 16411–16423.
- (49) Vračar, L.; Krstajić, N.; Neophytides, S. G.; Jakšić, J. Underpotential Deposition of Hydrogen on MoPt<sub>4</sub> Intermetallic Phase in Acid Solution: Temperature Dependence. *Int. J. Hydrogen Energy* **2004**, *29*, 835–842.
- (50) Zosimova, P. A.; Smirnov, A. V.; Nesterenko, S. N.; Yuschenko, V. V.; Sinkler, W.; Kocal, J.; Holmgren, J.; Ivanova, I. I. Synthesis, Characterization, and Sulfur Tolerance of

- Pt–MoO<sub>x</sub> Catalysts Prepared from Pt–Mo Alloy Precursors. *J. Phys. Chem. C* **2007**, *111*, 14790–14798.
- (51) Wang, S.; Sawada, H.; Chen, Q.; Han, G. G. D.; Allen, C.; Kirkland, A. I.; Warner, J. H. In Situ Atomic-Scale Studies of the Formation of Epitaxial Pt Nanocrystals on Monolayer Molybdenum Disulfide. *ACS Nano* **2017**, *11*, 9057–9067.
- (52) Ferreira, P. J.; la O', G. J.; Shao-Horn, Y.; Morgan, D.; Makharia, R.; Kocha, S.; Gasteiger, H. A. Instability of Pt/C Electrocatalysts in Proton Exchange Membrane Fuel Cells: A Mechanistic Investigation. *J. Electrochem. Soc.* 2005, *152*, A2256–A2271.
- (53) Lee, C.; Yan, H.; Brus, L. E.; Heinz, T. F.; Hone, J.; Ryu, S. Anomalous Lattice Vibrations of Single- and Few-Layer MoS<sub>2</sub>. *ACS Nano* **2010**, *4*, 2695–2700.
- (54) Rice, C.; Young, R. J.; Zan, R.; Bangert, U.; Wolverson, D.; Georgiou, T.; Jalil, R.; Novoselov, K. S. Raman-Scattering Measurements and First-Principles Calculations of Strain-Induced Phonon Shifts in Monolayer MoS<sub>2</sub>. *Phys. Rev. B* **2013**, *87*, 081307.
- (55) Chakraborty, B.; Bera, A.; Muthu, D. V. S.; Bhowmick, S.; Waghmare, U. V.; Sood, A. K. Symmetry-Dependent Phonon Renormalization in Monolayer MoS<sub>2</sub> Transistor. *Phys. Rev. B* **2012**, *85*, 161403.
- (56) Qiu, H.; Xu, T.; Wang, Z.; Ren, W.; Nan, H.; Ni, Z.; Chen, Q.; Yuan, S.; Miao, F.; Song, F.; Long, G.; Shi, Y.; Sun, L.; Wang, J.; Wang, X. Hopping Transport through Defect-Induced Localized States in Molybdenum Disulphide. *Nat. Commun.* **2013**, *4*, 2642.
- (57) Cheng, Y. C.; Zhang, Q. Y.; Schwingenschlögl, U. Valley Polarization in Magnetically Doped Single-Layer Transition-Metal Dichalcogenides. *Phys. Rev. B* **2014**, *89*, 155429.
- (58) Wang, S.; Wang, X.; Warner, J. H. All Chemical Vapor Deposition Growth of MoS<sub>2</sub>:h-BN Vertical van der Waals Heterostructures. *ACS Nano* **2015**, *9*, 5246–5254.



- (59) Xu, W.; Kozawa, D.; Liu, Y.; Sheng, Y.; Wei, K.; Koman, V. B.; Wang, S.; Wang, X.; Jiang, T.; Strano, M. S.; Warner, J. H. Determining the Optimized Interlayer Separation Distance in Vertical Stacked 2D WS<sub>2</sub>:hBN:MoS<sub>2</sub> Heterostructures for Exciton Energy Transfer. *Small* **2018**, *14*, 1703727.
- (60) Nan, H.; Wang, Z.; Wang, W.; Liang, Z.; Lu, Y.; Chen, Q.; He, D.; Tan, P.; Miao, F.; Wang, X.; Wang, J.; Ni, Z. Strong Photoluminescence Enhancement of MoS<sub>2</sub> through Defect Engineering and Oxygen Bonding. *ACS Nano* **2014**, *8*, 5738–5745.
- (61) Tiwari, J. N.; Sultan, S.; Myung, C. W.; Yoon, T.; Li, N.; Ha, M.; Harzandi, A. M.; Park, H. J.; Kim, D. Y.; Chandrasekaran, S. S.; Lee, W. G.; Vij, V.; Kang, H.; Shin, T. J.; Shin, H. S.; Lee, G.; Lee, Z.; Kim, K. S. Multicomponent Electrocatalyst with Ultralow Pt Loading and High Hydrogen Evolution Activity. *Nat. Energy* **2018**, *3*, 773–782.
- (62) Jagminas, A.; Naujokaitis, A.; Žalnėravičius, R.; Jasulaitiene, V.; Valušis, G. Tuning the Activity of Nanoplatelet MoS<sub>2</sub>-Based Catalyst for Efficient Hydrogen Evolution via Electrochemical Decoration with Pt Nanoparticles. *Appl. Surf. Sci.* **2016**, *385*, 56–62.
- (63) Jagminas, A.; Naujokaitis, A.; Žalnėravičius, R.; Jasulaitiene, V.; Valušis, G. Tuning the Activity of Nanoplatelet MoS<sub>2</sub>-Based Catalyst for Efficient Hydrogen Evolution via Electrochemical Decoration with Pt Nanoparticles. *Appl. Surf. Sci.* **2016**, *385*, 56–62.
- (64) Lazar, P.; Otyepka, M. Role of the Edge Properties in the Hydrogen Evolution Reaction on MoS<sub>2</sub>. *Chem. Eur. J.* **2017**, *23*, 4863–4869.
- (65) Li, L.; Qin, Z.; Ries, L.; Hong, S.; Michel, T.; Yang, J.; Salameh, C.; Bechelany, M.; Miele, P.; Kaplan, D.; Chhowalla, M.; Voiry, D. Role of Sulfur Vacancies and Undercoordinated Mo Regions in MoS<sub>2</sub> Nanosheets toward the Evolution of Hydrogen. *ACS Nano* **2019**, *13*, 6824–6834.

- (66) Yang, T. T.; Tan, T. L.; Saidi, W. A. High Activity toward the Hydrogen Evolution Reaction on the Edges of MoS<sub>2</sub>-Supported Platinum Nanoclusters Using Cluster Expansion and Electrochemical Modeling. *Chem. Mater.* **2020**, *32*, 1315–1321.
- (67) Trasatti, S. Work Function, Electronegativity, and Electrochemical Behaviour of Metals: III. Electrolytic Hydrogen Evolution in Acid Solutions. *J. Electroanal. Chem. Interfacial Electrochem.* **1972**, *39*, 163–184.
- (68) Paciok, P.; Schalenbach, M.; Carmo, M.; Stolten, D. On the Mobility of Carbon-Supported Platinum Nanoparticles towards Unveiling Cathode Degradation in Water Electrolysis. *J. Power Sources* **2017**, *365*, 53–60.
- (69) Murthy, A. P.; Theerthagiri, J.; Madhavan, J.; Murugan, K. Highly Active MoS<sub>2</sub>/Carbon Electrocatalysts for the Hydrogen Evolution Reaction – Insight into the Effect of the Internal Resistance and Roughness Factor on the Tafel Slope. *Phys. Chem. Chem. Phys.* **2017**, *19*, 1988–1998.
- (70) Nagasubramanian, G. Two- and Three-Electrode Impedance Studies on 18650 Li-Ion Cells. *J. Power Sources* **2000**, *87*, 226–229.
- (71) Xu, W.; Kozawa, D.; Zhou, Y.; Wang, Y.; Sheng, Y.; Jiang, T.; Strano, M. S.; Warner, J. H. Controlling Photoluminescence Enhancement and Energy Transfer in WS<sub>2</sub>:hBN:WS<sub>2</sub> Vertical Stacks by Precise Interlayer Distances. *Small* **2019**, *16*, 1905985.
- (72) Tsai, C.; Abild-Pedersen, F.; Nørskov, J. K. Tuning the MoS<sub>2</sub> Edge-Site Activity for Hydrogen Evolution via Support Interactions. *Nano Lett.* **2014**, *14*, 1381–1387.
- (73) Wang, S.; Rong, Y.; Fan, Y.; Pacios, M.; Bhaskaran, H.; He, K.; Warner, J. H. Shape Evolution of Monolayer MoS<sub>2</sub> Crystals Grown by Chemical Vapor Deposition. *Chem. Mater.* **2014**, *26*, 6371–6379.

## ToC Graphic

